Universiteit Utrecht

Generalized Causal Dynamical Triangulations in two dimensions

Master Thesis Theoretical Physics and Mathematical Sciences
August 2012

Author:
Renee Hoekzema
renee.hoekzema@earth.ox.ac.uk

Supervisors:
Prof. Renate Loll, Utrecht University
Prof. Tom Ilmanen, ETH Zürich
Prof. Gunther Cornelissen, Utrecht University

Abstract

In this thesis we describe a generalization of two-dimensional Causal Dynamical Triangulations (CDT) that relaxes the time-layering condition and was introduced by Jordan [32]. We present two closely related models which we call bubble generalized CDT (gCDT) and spiral gCDT and we set the first steps towards finding an analytical solution to both of the models. After reformulating the method of solving two-dimensional CDT analytically via the transfer matrices, as presented in [13], we devise a similar approach for the bubble gCDT model. We perform the first calculations towards building several simplified versions of the model. We then introduce the framework of matrix models in order to formulate the CDT matrix model that was introduced in [15] and present a generalization for spiral gCDT. We finish with a general discussion of other approaches to gCDT in two dimensions.

Painting on the cover by Anneke Kerkhof

Contents

Introduction

This thesis is the result of a combined research project for a double masters degree in Theoretical Physics and Mathematical Sciences at Utrecht University. I was supervised by Professor Renate Loll from the Theoretical Physics Department in Utrecht and Professor Tom Ilmanen from the Mathematics Department at the ETH Zürich. Professor Gunther Cornelissen was my second mathematics supervisor at Utrecht University. The topic of my research and this thesis is Quantum Gravity, in particular a two-dimensional version of a new generalization of Causal Dynamical Triangulations (CDT), that relaxes the time-layering condition of this non-perturbative approach to Quantum Gravity. The model was proposed by Samo Jordan [32].

The unification of Einstein's theory of gravity and quantum theory is a problem that has eluded physicists ever since both theories were first developed, almost 100 years ago. In expectation of a combined theory, the research in the field is known as Quantum Gravity. For an introduction to the problems encountered in this field I would recommend Christopher Isham's articles [29, 30, 31].
The gravitational path integral is an approach to Quantum Gravity that is straightforward in intention, but hard to define concretely. The problem lies mainly in the definition of a set of geometrical spaces, the *space of geometries*, and a measure thereon, that are superposed via an integral and weighted by the Einstein-Hilbert functional. CDT is a non-perturbative approach to Quantum Gravity in which the space of geometries and the path integral are explicitly constructed as the continuum limit of a sum over weighted discrete geometrical spaces [11, 12, 7]. These discrete geometries are built up out of simplices and have strict time-layering such that every spatial hypersurface has the same topology. This construction turns out to have very promising results in two, three and four dimensions. The method seems to deliver the classically expected de Sitter space as its average geometry, as weighted by its path sum and computed using computer simulations.
If one does not require such a time-layering, but allows for any triangulation, the nice behaviour does not present itself in three and four dimensions. We call this approach Dynamical Triangulations (DT) and a summary of the results can be found in [36]. It would seem that a typical geometry in the continuum limit even has a wrong macroscopic dimension. This raises the interesting question what it is that makes CDT work while DT does not. The difference seems to lie in the change of spatial topology, which is disallowed in CDT but not in DT [4, 3].
A change of spatial topology in a Lorentzian space violates causality, in the sense that the light cones, the future and past at a point, are not well defined on the branching point of the space, which we call a Morse point [24]. In CDT the change of topology of the spatial hypersurfaces is explicitly disallowed. But instead of these strict conditions of time-layering and excluded topology change, one can also prevent spatial topology change by solely requiring the light cone to be well defined at every vertex of the configuration. In order to do this one should endow the edges of the configuration with a colour representing their character, either timelike or spacelike. In section 2.3 we will discuss why this is a sensible thing to do. In two dimensions demanding a light cone to be well-defined then becomes straightforward. At every vertex, there should be timelike edges pointing up and down and spacelike edges to either side. We call this the light cone colouring condition. The two two-dimensional models of generalized CDT (gCDT) that we will present in this thesis are based on this assumption.
As CDT can be solved analytically in two dimensions, the question arises whether the same is possible for a generalized model that satisfies the light cone colouring condition. The

quest for such a solution is the main topic of this thesis.

In the first chapter we introduce the problem of finding a discretization for the gravitational path integral in two dimensions. Section 2.1 introduces CDT and shows that two-dimensional CDT can also been seen as a model that locally satisfies a restricted version of the light cone colouring condition. In the second section of Chapter 2 we propose two related two-dimensional gCDT models, bubble gCDT and spiral gCDT, and prove some interesting properties of the associated configurations. The third section concerns the relation between a triangle in Euclidean space and a triangle in Minkowski space and shows why it is not a bad idea to associate characters to the edges of the triangle.
Chapter 3 reformulates the method of strip propagators or transfer matrices that can be used to solve two-dimensional CDT analytically. We construct a similar approach for bubble gCDT and explore the options for solving or simplifying this model.
In Chapter 4 we submerge ourselves in the world of matrix models. After an introduction to the required techniques we present a slight adaptation of the matrix model for CDT introduced by Benedetti and Henson in [15]. We propose a generalized matrix model that would generate the spiral gCDT configurations with appropriate weights and discuss possible methods for solving either model. Both CDT and spiral gCDT have another dual representation as a matrix model and we briefly discuss these as well.
Chapter 5 discusses a few other approaches to the problem of solving two-dimensional gCDT.

1 Quantum Gravity

1.1 The Gravitational Path Integral

1.1.1 Introducing the Gravitational Path Integral

The aim when trying to construct a theory of Quantum Gravity is to build a mathematical model describing gravitational interactions at the shortest scales and highest energies, that is internally consistent, but also yields the right limiting behaviour in the classical gravitational regime. We would like it to both capture the probabalistic nature of quantum theories and at the same time preserve some of the geometrical beauty of General Relativity (GR). The gravitational path integral is one way to express this desire. One might view the path integral itself, the weighted superposition of all possible options, as the essence of a quantum theory, and the study of the geometrical Einstein-Hilbert action as the essence of GR. We can then formulate the wish to unite the two as follows:

$$Z(G_N, \Lambda) = \int_{\mathcal{G}(M)} \mathcal{D}g \, e^{iS_{EH}[g]}, \tag{1}$$

where we integrate over $\mathcal{G}(M)$, the space of all distinct geometries that we want to superpose on the n-dimensional base manifold M. In the exponent we meet the Einstein-Hilbert action

$$S_{EH}[g] = \frac{1}{16\pi G_N} \int_M d^n x \sqrt{-g} \, (R - 2\Lambda) \, . \tag{2}$$

Here R is the Ricci curvature of the geometry g, Λ is the cosmological constant and G_N is Newton's gravitational constant. The measure $d^n x\sqrt{-g}$ stands for the volume measure, where now we also write g for the determinant of the geometry g written out as a bilinear form on the tangent space of M in a particular set of coordinates. Since this determinant g and R are both scalar in a tensorial sense and therefore independent of coordinates, S_{EH} is a well-defined function from $\mathcal{G}(M)$ to $\mathbb{R}$. The entire path integral, however, is not at all well-defined. For most choices of the space of geometries $\mathcal{G}$, it is neither clear how to parametrize $\mathcal{G}$, nor what kind of measure to define on it. Even if we consider only smooth inequivalent Lorentzian metrics "$\mathrm{Lor}(M)/\mathrm{Diff}(M)$", one cannot straightforwardly make sense of the expression.

1.1.2 How to solve a path integral

The path integral formulation of Quantum Mechanics introduced by Feynman considers the weighted superposition of all paths a particle can travel. Defining a measure on this space of all paths brings similar difficulties as defining a measure on the space of geometries for the case of the gravitational path integral. In Quantum Mechanics one solves this problem by Wick rotating the time variable, considering piecewise linear paths as illustrated in Figure 1.1, performing the discretized path integral, taking a continuum limit and Wick rotating back.
We would like to construct an analogous approach for the gravitational path integral. Wick rotation transforms the phase factor in the path integral to a genuine weight factor by rotating the time variable in the complex plane towards "imaginary time", $t \to i\tau$. We can then interpret the path integral as an unnormalized probability functional.
The space of geometries can be discretized by considering piecewise flat geometries with N building blocks of a certain type or multiple types. We then study the discretized path integral and try to find a well-behaved $N \to \infty$ continuum limit for suitable values of the coupling constants. In the end we Wick rotate back.

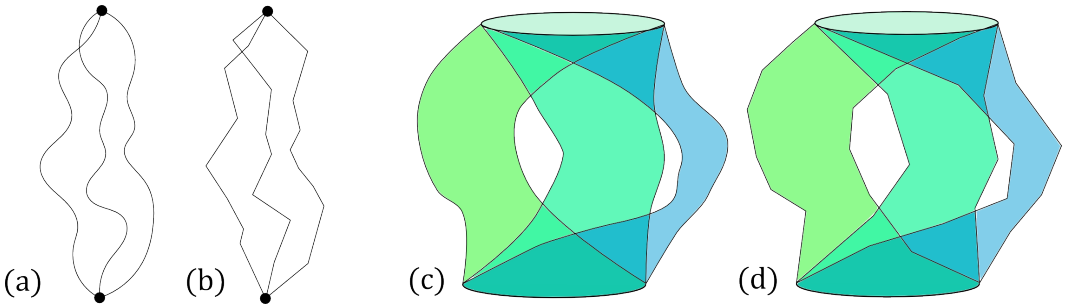

Figure 1.1: An illustration of the space of geometries for a path integral with given boundaries. In Quantum Mechanics we want to approximate a space of paths between the boundary points as illustrated in (a) and we do this by discretizing to piecewise linear paths (b) and taking an infinite refinement limit. In the gravitational path integral we similarly wish to construct a space of higher-dimensional geometries (c) and we choose a set of discretized geometries (d) and try to find an appropriate continuum limit.

1.1.3 What discretization to choose

In the case of Quantum Mechanics, the paths are discretized by considering piecewise linear paths with a fixed number of pieces. One then takes the limit of the number of pieces going to infinity. There is little freedom to choose this discretization because we are working in one dimension. In the higher-dimensional gravitational path integral however, many different discretizations of the space of geometries are possible, so the question is which one to take. The choice of a discrete model might now seem like an arbitrary parameter influencing the behaviour of the eventual theory, but luckily *universality* presents a force to counteract the influence of this choice. Universality is a general concept that appears in many systems with a large number of variables, where one considers the effective behaviour in the limit where the number of variables grows. It states that, if a well-defined limit exists, in many cases slight, or even major adjustments to the system affect the behaviour of this limit very little or not at all. In the case of a continuum limit of discretized weighted spaces, it means that many different discrete models will flow towards the same continuum theory if a continuum limit can be defined at all. We have illustrated this behaviour in Figure 1.2.
Giving meaning to the gravitational path integral as a theory of Quantum Gravity now comes down to building a discrete ensemble of piecewise linear geometries, such that its universality class has a continuum limit with the right behaviour:

(i) There is a way to study the dynamics of the continuum theory;

(ii) We can construct an "average spacetime" by studying the expectation values of suitable observables and on large scales this resembles a classical spacetime;

(iii) On short scales we expect exotic"quantum fluctuations" of geometry.

This is a method of building a Quantum Gravity theory that is in principle constructive. In the continuum limit of the discrete ensembles, a certain space of geometries is constructed together with a measure and a probability functional on it, such that they satisfy our requirements. This does not deliver a direct description or *effective theory* of this space or the behaviour of the functional itself.

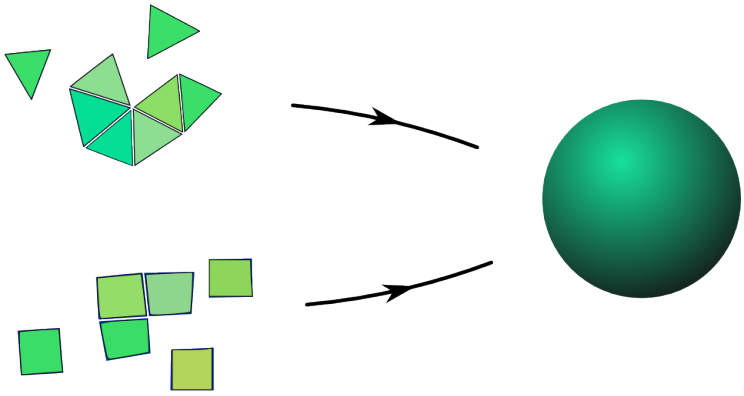

Figure 1.2: Different discrete models can, in the presence of a well-defined continuum limit, yield the same continuum theory. For example using either triangles or squares as basic building blocks in a particular two-dimensional discrete model, will in general yield the same continuum theory, if there is one.

1.2 The path sum in two dimensions

In this thesis we will be studying the two-dimensional gravitational path integral and in this section we work out the method for solving it in more detail.

1.2.1 From path integral to path sum

We Wick rotate the two-dimensional path integral and work in a Euclidean framework. Wick rotation changes the relative sign of the kinetic and potential terms in the Euclidean Einstein-Hilbert action, so the two-dimensional Euclidean path integral looks as follows:

$$S_{EH}^{\text{Eucl}}[g] = \frac{1}{16\pi G_N} \int_M d^2x\sqrt{g}\ (R + 2\Lambda)\,, \tag{3}$$

where g now is a Riemannian geometry on M. We define a family $\mathcal{T}_N$ of distinct allowed geometries with N unlabelled building blocks, each with a flat Euclidean geometry. Suppose for simplicity that these building blocks are all polygons of equal area A. Gluing them together gives us a polygonization of M with a piecewise flat geometry on M inherited from the geometries of the individual building blocks. Because we are dealing with a polygonization, all curvature is located at the $(n-2)$-bones of the structure. In this case it is located in pointlike, conical curvature singularities at the vertices. The integral over the internal curvature therefore becomes a sum over the deficit angles at every internal vertex:

$$\int_M d^2x\sqrt{g}\, R = \sum_{s\in S_0} (2\pi - \phi_s)\,. \tag{4}$$

Here S_0 is the 0-skeleton (the set of vertices) of the polygonization and ϕ_s is the sum over the internal angles at the vertex s.
If M has a boundary, then in order to make the action additive under gluing two polygonizations along their edge, we need to add a boundary term. This is the integral over the geodesic curvature k_g along the boundary, which in the discrete case becomes the sum over

the angles of the "kinks" in the boundary.

$$\int_{\partial M} d^2x\sqrt{g}\, k_g = \sum_{s\in S_0^{\partial M}} (\pi - \phi_s)\,, \tag{5}$$

where $S_0^{\partial M}$ is the collection of boundary vertices. The Gauss-Bonnet formula tells us that in two dimensions, adding this boundary curvature term to the internal curvature term gives us precisely a topological constant.

$$\int_M d^2x\sqrt{g}\, R + \int_{\partial M} d^2x\sqrt{g}\, k_g = 2\pi\chi(M) \tag{6}$$

Here $\chi(M)$ is the Euler characteristic that depends only on the homotopy class of M. Taken together with the cosmological term, the Einstein-Hilbert action therefore reduces to the two-dimensional *Regge action* [39].

$$S_{Regge}(T) = \frac{1}{16\pi G_N}\left(2\pi\chi(T) + 2\Lambda\, Area(T)\right), \tag{7}$$

for $T \in \mathcal{T}_N$. The Euclidean path integral can now in theory be written as the $N \to \infty$ continuum limit of the path sum for fixed volume, if such a limit exists:

$$Z = \lim_{N\to\infty} \sum_{T\in\mathcal{T}_N} \frac{1}{C_T} e^{-S_{Regge}(T)}. \tag{8}$$

The factor C_T is the order of the symmetry group of the configuration T. We divide out this factor because the gauge orbit of symmetric configurations is smaller than that of asymmetric configurations when we divide out labelling from a set of labelled configurations and we want the measure we construct to take this into account.

1.2.2 The existence of a continuum limit

If we work with a base manifold M for every configuration, then the curvature term is constant, so we can ignore it in the path integral. We have:

$$Z \propto \lim_{N\to\infty} \sum_{T\in\mathcal{T}_N} \frac{1}{C_T} e^{-\frac{\Lambda}{8\pi G_N} Area(T)} \sim \lim_{N\to\infty} \sum_{T\in\mathcal{T}_N} e^{-\lambda\, A\, N}, \tag{9}$$

where we have defined $\lambda = \frac{\Lambda}{8\pi G_N}$ and in the last step we make use of the fact that as the configurations grow larger, relatively fewer will have an overall symmetry, so the factor C_T can be neglected in the limit. We take the area A of the individual building blocks to be constant as N varies, such that the $N \to \infty$ limit corresponds to the infinite-volume limit of the configurations. We see here that in two dimensions, the difficulty of solving the path integral lies not within the weight itself, which is very simple, but in controlling the sum over all possible configurations. It is now clear that for such a model, an infinite-volume limit exists precisely if the number of elements of $\mathcal{T}_N$ grows exponentially with N, with some exponent λ_{crit}, such that

$$\lim_{N\to\infty} \sum_{T\in\mathcal{T}_N} e^{-\lambda\, A\, N} \sim \lim_{N\to\infty} e^{\lambda_{crit}\, N} e^{-\lambda\, A\, N}, \tag{10}$$

and there is a critical point at $\lambda\, A = \lambda_{crit}$. Whether this limit gives rise to an interesting continuum theory is a different question and has to be explored separately.

Instead of the $N \to \infty$ limit, one can also consider the grand canonical ensemble, where we let the number of building blocks N vary.

$$Z \sim \sum_N \sum_{T \in \mathcal{T}_N} e^{-\lambda A N} = \sum_{T \in \mathcal{T}} e^{-\lambda A N(T)}, \tag{11}$$

where $\mathcal{T} = \bigcup_N \mathcal{T}_N$. Because a negative exponential is a summable function, this sum will exhibit the same critical behaviour.
Once we have calculated the limit of the path sum and its critical exponent, we can probe what the average geometry looks like by taking derivatives of the path integral or calculating expectation values of suitable observables. In the end we make sure to Wick rotate back in order to obtain, in theory[1], results for Lorentzian spaces.

1.3 Dynamical Triangulations

It is convenient to use triangles as basic building blocks to build our discrete geometries, or in higher dimensions simplices. These have the smallest angles of all polygons or polytopes and therefore can approximate curvature most accurately. How curvature is approximated by triangles is illustrated in Figure 1.3.

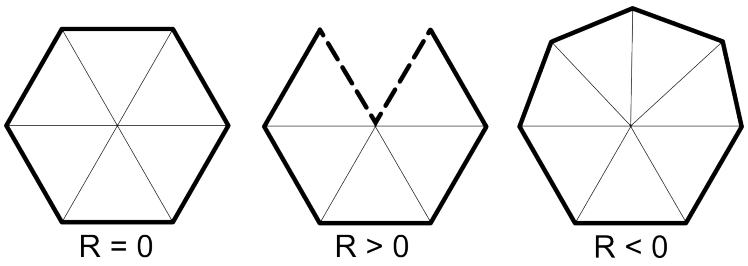

Figure 1.3: Gluing six equilateral triangles together yields a flat surface (left). If we leave out one or more of them, we obtain a positively curved cone (middle), and gluing more than six together yields a negatively curved saddle shape (right).

Dynamical Triangulations (DT) is the most straightforward model within this approach. As basic building blocks we use Euclidean equilateral triangles or, in higher dimensions, equilateral simplices. It was initially introduced to study string theory and two-dimensional quantum gravity [19, 5]. A brief summary of the method can be found in [36]. In two dimensions the continuum behaviour comes out right and we obtain Liouville gravity. In higher dimensions however, DT does not give us the right large scale behaviour in the continuum limit. The average geometry will even have the wrong macroscopic dimension [1, 10].

[1] This is not entirely straightforward because Wick rotation is not a one-to-one correspondence between Riemannian and Lorentzian geometries. [37] discusses Wick rotation and its status in CDT.

2 CDT and gCDT

For an introduction to the terminology and basics of graph theory and directed graphs I refer to [17] and [14].

2.1 Causal Dynamical Triangulations

2.1.1 Introduction to CDT

Causal Dynamical Triangulations, as introduced by Loll and Ambjørn in [13], is a modification of DT where the set of allowed triangulations $\mathcal{T}$ is restricted to consist of only triangulations with a strict *time-layering*. This means that there is a family of hypersurfaces, that we call *spatial*, in the triangulation, that all have the same topology and are separated by a single slice of the triangulation. All simplices are between two of these layers, so the layers contain all the vertices of the triangulation.
It turns out that restricting our set of triangulations in this way brings us to a different universality class of models which moreover in $d > 2$ exhibit exactly the desired behaviour in the continuum limit. In four dimensions, there is a phase in the phase diagram of our coupling constants in which the geometries are on average four dimensional and shaped like a de Sitter space, which is exactly the expected classical behaviour [8]. On small scales, the dimension seems to go down to two, thus revealing a hint of highly non-classical behaviour in the geometry near the Planck scale.

2.1.2 CDT in two dimensions

In two-dimensional CDT we use a closed cylinder as the underlying manifold for our triangulations. The spatial layers are now circles and the triangulations in between are annuli that do not contain vertices. In Figure 2.1 we see an example of a two-dimensional CDT triangulation. We encounter two types of edges, which we can endow with two different labels or colours. The edges within the spatial circles we colour "s" for *spacelike* and the internal edges of the annuli we colour "t" for *timelike*.

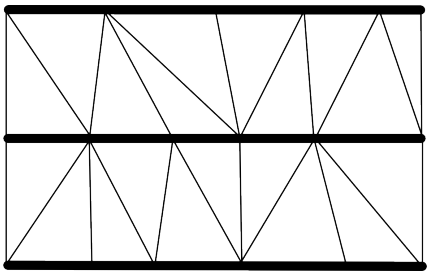

Figure 2.1: An example of a two-dimensional CDT triangulation on a cylinder, where the two sides should be identified.

Definition 2.1. A **bicoloured triangulation** is a finite, regular triangulation whose edges are partitioned into two sets (colours). By regular we mean that the triangulation is a topological manifold, although in this thesis we may sometimes allow for the two boundaries loops of a triangulated cylinder to (partially) overlap (which we call "collapsed boundaries").

Note that because the Euler characteristic is invariant under homotopy, it does not matter for the curvature term in the action whether the two boundaries of a cylinder touch each other or not, even though the topology is different.
We now give the following formal definition of a coloured CDT triangulation in two dimensions:

Definition 2.2. A **two-dimensional CDT triangulation** is a bicoloured triangulation of a cylinder satisfying the following conditions:

(i) (*tts*): Every triangle has two timelike (t) edges and one spacelike (s) edge;

(ii) (*Timeslicing*): Cutting along all spatial edges partitions the triangulations into *strips*: triangulations of an annulus with only spatial edges on the boundary loops and only timelike edges in the interior;

(iii) (*No topology change*): The way the strips are glued together defines a linear order on them, and we label the initial and the final strip (such that the two directions of the linear order define different configurations).

There is another way to describe these triangulations in terms of more local conditions, and this was used in [15] to formulate a matrix model that generates the CDT path sum, which will be described in Chapter 4.

Definition 2.3. A **locally generated CDT triangulation** is a non-empty bicoloured triangulation satisfying:

(i) (*tts*): Every triangle has two t-edges and one s-edge;

(ii) (*Colouring condition*): Every vertex has precisely two adjacent s-edges;

(iii) (*Boundary condition*): The boundary of the triangulation consists of two circles of colour s, one of which is labelled initial and the other final.

Figure 2.2 illustrates the first two conditions in this definition.

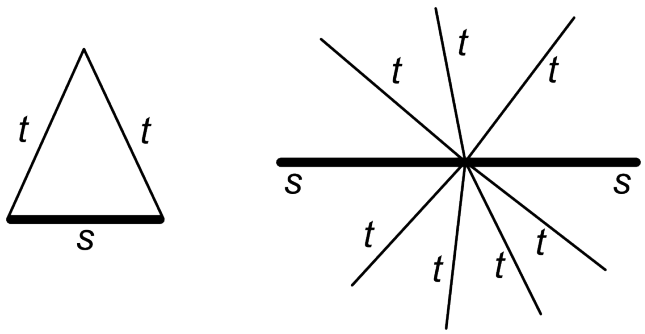

Figure 2.2: Illustration of the local conditions that generate locally generated CDT. The *tts* condition (left) and the colouring condition (right).

Lemma 2.4. *The set of locally generated CDT triangulations is equal to the set of CDT triangulations.*

Proof. Both ensembles are built out of *tts*-triangles.

First we show that the CDT conditions on a cylindrical surface imply 2.3(ii) and 2.3(iii). A CDT triangulation can be partitioned into strips which are glued according to a linear order. Since the triangulation is finite, there must be a first and last strip. The boundaries of these strips are spatial loops, thus implying condition 2.3(iii). Because of the (*tts*) condition, all vertices in a strip must be on the boundary of the strip. Therefore every vertex is either on the boundary between two adjacent strips, or on the boundary of the triangulation. In either case, the colouring condition 2.3(ii) holds.

Now we show that definition 2.3 of locally generated CDT triangulations implies 2.2(ii) and 2.2(iii) and cylindrical topology. Spatial topology change requires a Morse point, see for example [24], which would require more than two spatial edges and is therefore excluded by the colouring condition. See Figure 2.3 for illustration of the argument. Since the spatial topology of the two boundary loops is a circle, all spatial hypersurfaces have the topology of a circle. Note that here the boundary condition excludes the formation of spirals. As there are only *tts*-triangles and there is no timelike boundary, all triangles must lie in strips between two spatial circles. Collecting the information that there is no topology change, that the triangulation is finite and that it has two loops at the boundary, we can conclude that the topology must be cylindrical and the strips can be endowed with a linear gluing order.

□

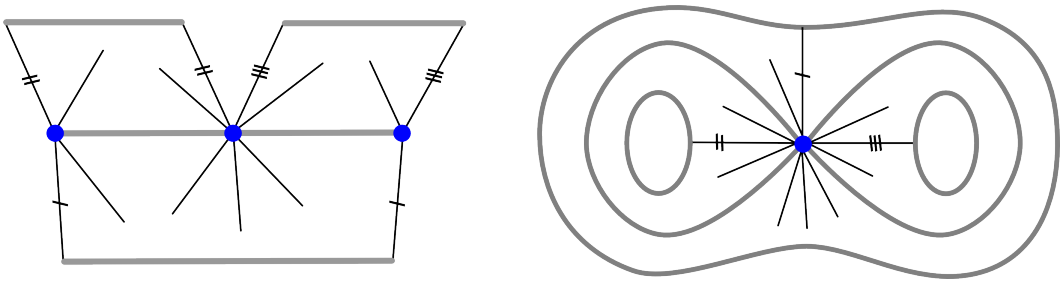

Figure 2.3: Change in the spatial topology of a configuration requires a Morse point. We depict here an impression of a CDT strip that splits into two strips. On the left we represent the configuration projected as before, with the corresponding gluing lines marked accordingly. On the right we have glued the configuration along the marked edges. We see that the splitting vertex, marked blue, is connected to four spatial lines, here shown in gray, thus violating the colouring condition.

So we see that CDT in two dimensions indeed has a nice local description, which we will need for the formulation of CDT as a matrix model in Chapter 4.

2.2 Generalized Causal Dynamical Triangulations

2.2.1 Introduction to gCDT

Generalized Causal Dynamical Triangulations (gCDT), a model introduced by Jordan [32], relaxes the strict time-layering condition of CDT, while keeping an element of "causality" in the definition. The two-dimensional version of gCDT is the central topic of this thesis. We will define two different models that generalize two-dimensional CDT, which we call

bubble gCDT and *spiral gCDT*. Both of these make use of the addition of a new triangle with colouring *sst*, and a generalization of the vertex colouring condition we saw in the previous section. The new *light cone colouring condition* states that at every vertex there are timelike edges above and below and spacelike edges on either side, as is illustrated in Figure 2.4.

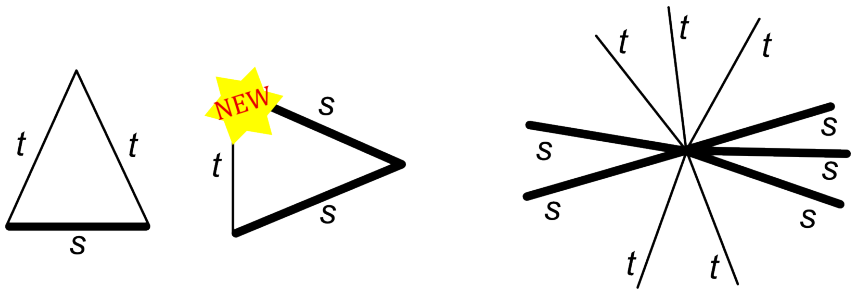

Figure 2.4: In two-dimensional gCDT we deal with both the *tts*- and *sst*-triangles and a light cone vertex colouring condition as depicted above.

A typical configuration now has added structure on top of the strips that were present in CDT, as is illustrated in Figure 2.5.

2.2.2 Why generalize CDT?

There are various reasons why it is very interesting to study a generalization of CDT that relaxes the time-layering condition. In CDT all spatial hypersurfaces have equal timelike separation, and transition amplitudes can be calculated between two of these layers. In a theory of Quantum Gravity, one of the goals would eventually be to be able to calculate transition amplitudes between any two separated spatial hypersurfaces. Previously there have already been attempts to locally increase the timelike separation of spatial hypersurfaces in CDT by introducing wedges, and this did not alter the universality class of the model. In gCDT this is generalized even further.
The time-layering of CDT is often criticized to be a very rigid structure. It would be nice to study the role it plays in the results of CDT. By relaxing this condition, but not in a way that brings us back to Dynamical Triangulations, and studying whether the resulting continuum theory also has nice features, we can try to understand in what sense the strict layering is necessary for CDT. If it is the lack of spatial topology change that plays a role as has been suggested, then perhaps gCDT will present similar results, because, as we will

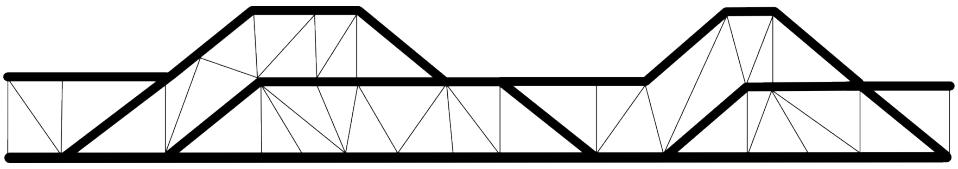

Figure 2.5: Example of a gCDT configuration. The thin edges are timelike and the fat edges are spacelike. The sides should be identified to obtain a cylinder topology. We see that the spatial circles of CDT are decorated with spatial "bubbles" (see section 2.2.3).

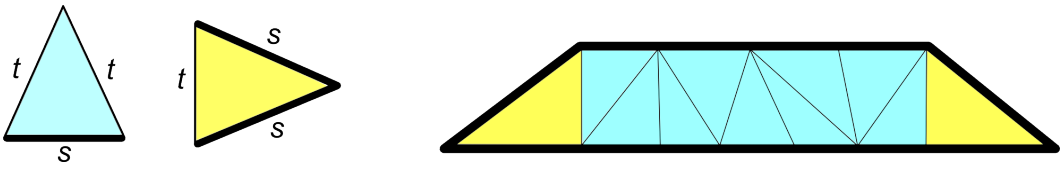

Figure 2.6: A bubble contains two *sst*-triangles (yellow) and any number of *tts*-triangles (blue).

see in the next few subsections, spatial topology is also excluded by the light cone colouring condition.
The gCDT models in two and more dimensions will have more freedom than CDT. By this we mean that there are more different configurations with the same number of building blocks, because there are now more different building blocks and there are more allowed ways to glue them to each other. This might mean that the continuum results are better approximated with a smaller number of building blocks, which would be good news for the Monte Carlo simulations that are used to study CDT in higher dimensions, for which computational force is a limiting factor.
In two dimensions specifically, we note that the spiral gCDT model that will be introduced below, restores the local symmetry between space and time that is also present in Minkowski space. This illustrates that if gCDT were to present results that are similar to the results of CDT, then this could shed some light on the connection between CDT and theories that explicitly separate space and time, such as Hořava-Lifshitz theory. See [28] for an introduction to the latter and [6] for its connection to CDT.

2.2.3 Bubble gCDT

In bubble gCDT we add to a CDT triangulation structures that we call *bubbles*. They consist of two *sst*-triangles on either side and any number of *tts*-triangles in between, as illustrated in Figure 2.6.

Definition 2.5. The **spatial or timelike skeleton** of a CDT or gCDT configuration is the collection of s- or t-edges respectively, together with the attached vertices.

In the bubble gCDT model we require that all configurations can be obtained by gluing bubbles and strips on top of each other one by one. This makes sure that we can define *bubble time*, a linear order of spatial circles of which every s-edge is a part. In general there are multiple ways to define bubble time on a configuration. Its definition is unique precisely if there is a unique order of gluing the bubbles. An example of a bubble gCDT configuration for which there is no unique definition of bubble time is shown in Figure 2.7.
We note that the configurations of bubble gCDT can be obtained from the CDT triangulations, both by decorating spatial layers with bubbles or by collapsing strips to form bubbles. In the case of the first, we should add the empty triangulations with completely collapsed boundaries, that consist of a single ring of vertices, to the set of CDT configurations. Otherwise one cannot obtain the bubble gCDT configurations whose spatial skeleton is connected from the set of CDT triangulations. Note that because the Euler characteristic is homotopy invariant, this does not affect the curvature term. In bubble gCDT we will also allow for the initial and final boundary of the triangulation to overlap, partially or completely. We will be studying this model in Chapter 3.

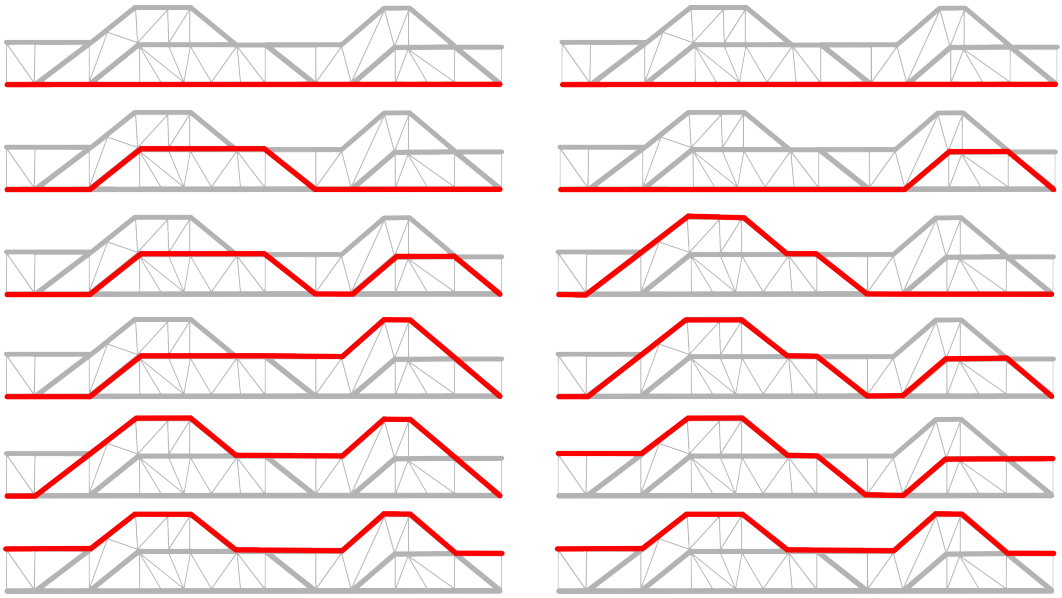

Figure 2.7: This figure illustrates two distinct ways to define bubble time on a given bubble gCDT triangulation. From top to bottom we define six subsequent slices of discrete time. These slices overlap partially. We see that this order of spatial circles can be defined on this configuration in (at least) two inequivalent ways.

2.2.4 Spiral gCDT

Spiral gCDT is the local symmetrization in s and t of locally defined CDT. It generalized bubble gCDT in the sense that it drops the gluing condition on the bubbles. Therefore all bubble gCDT configurations, and thus in particular all CDT configurations, are contained in the set of spiral gCDT configurations. In this model we will exclude triangulations with collapsed boundaries for simplicity, and assume all our bicoloured triangulation are topological manifolds.

Definition 2.6. A (locally generated) **spiral gCDT triangulation** is a bicoloured triangulation such that:

(i) (*tts and sst*): Every triangle has either two timelike (t) and one spacelike (s) side or two spacelike and one timelike (s) side;

(ii) (*Lightcone colouring condition*): When walking around a vertex we encounter every colour twice with any multiplicity, as illustrated in Figure 2.8, except for vertices on the boundary, which have no outward pointing t-edges;

(iii) (*Boundary condition*): The boundary consists of two spatial circles, one of which is labelled the initial boundary and the other the final boundary.

Because we are dropping the gluing condition of bubble gCDT, bubbles are now allowed to overlap themselves and form spirals, as illustrated in Figure 2.9a. Another structure that occurs are bubbles overlapping each other as in Figure 2.9b, so that the configuration cannot be constructed by gluing bubbles on top of each other one by one.
At every vertex the edges can be divided into two groups, the two *sides* of the vertex, divided by the spatial edges.

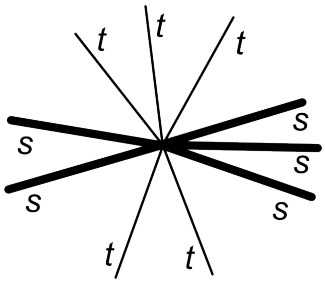

Figure 2.8: The light cone colouring condition that we impose as a local condition at the vertices in spiral gCDT.

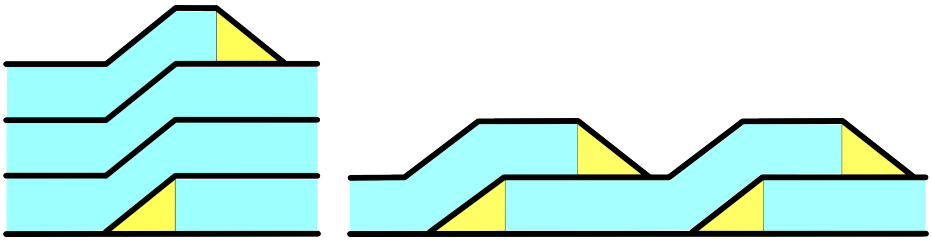

(a) Example of a spiral. (b) Example of two mutually overlapping bubbles.

Figure 2.9: Example of two spiral gCDT configurations that do not appear in bubble gCDT. Blue and yellow represent *tts*- and *sst*-triangles respectively and we leave out most of the timelike edges.

Definition 2.7. We define a **time walk** on a spiral gCDT configuration to be a directed walk along the timelike edges that, at every vertex, continues on the other side of the spatial edges.

The spiral gCDT configurations then satisfy a discrete version of the theorem about infinitely extendable timelike geodesics.

Lemma 2.8. *A time walk can always be continued unless we encounter a boundary.*

Proof. This is a direct consequence of the light cone colouring condition 2.6(ii). □

Interestingly, even though the spiral gCDT configurations are generated from very local conditions, they still have some nice properties that allow us to relate them to Lorentzian spaces. In particular, we can endow the set of vertices with a causal structure, which is a partial order that represents a time direction. We define this partial order via the timelike skeleton, which we transform into an acyclic directed graph (digraph). In order to do this we first have to check that it cannot happen that two time walks originating at the initial boundary hit the same vertex on either side, as illustrated in Figure 2.10.

Proposition 2.9. *In any spiral gCDT configuration, it cannot happen that two directed time walks away from the initial boundary end up at opposite sides of the spatial edges at a vertex.*

Proof. Suppose two time walks away from the initial boundary end up at opposite sides of a vertex v. We mark the two walks and the piece of boundary as illustrated

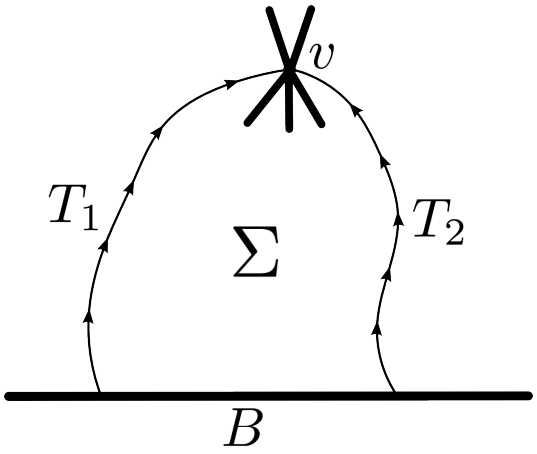

Figure 2.10: Illustration of the situation that is excluded by Proposition 2.9. Two time walks T_1 and T_2 are directed outward from the initial boundary and meet on opposite sides of the vertex v. This divides the boundary into two pieces, and we choose the piece B such that the surface Σ enclosed by T_1, T_2 and B does not contain the final boundary. The walks T_1 and T_2 and B are redefined a few times until we hit a contradiction.

in Figure 2.10. The piece of the boundary B is chosen such that the final boundary is not enclosed by the path C given by B, T_1 and T_2. The triangulation enclosed by C we call Σ.

First we eliminate the internal vertices of B. From every internal vertex of B originate time walks as defined in Definition 2.7. By Lemma 2.8, these do not end within Σ unless they return to B. If they return to B, then we can redefine T_1 and T_2 to be pieces of this path. We do this until there are no more walks from B returning to B within Σ.

Other time walks originating from B, that do not return to B, must now cross either T_1 or T_2 or connect to one of the sides of v. We can redefine T_1 and T_2 to (partially) follow these walks in Σ in such a way that B does not have any internal vertices left. We can do this because there is at least one timelike walk originating from every vertex of B and all of these can be used to redefine either T_1 or T_2 and make Σ smaller. Note that it might still be the case that B has an internal edge.

Claim *Σ has at least one internal vertex.*

Proof The vertex v per definition has at least one s-edge pointing inwards into Σ. This edge cannot be connected to T_1 or T_2 because this would violate either the triangulation condition or the colouring condition. It cannot connect to an internal vertex on B because we have eliminated those. Therefore it must connect to an internal vertex of Σ.

We pick an internal vertex w of Σ. We pick two opposite t-edges of w and extend them to a time walk γ, until they hit T_1, T_2, B or end up on either side of v. Using γ we can redefine T_1 and T_2 such that Σ has at least one internal vertex less, namely w. *Contradiction:* The entire triangulation and therefore Σ is finite, so repeating this procedure is in contradiction with the claim that Σ has at least one internal vertex.

□

Definition 2.10. We define the **timelike digraph** of a spiral gCDT configuration inductively in the following way:

(i) On the initial boundary we direct all timelike edges away from the boundary.

(ii) If a directed edge points toward a vertex, then we define the t-edges on that side of the s-edges of the vertex as incoming and the t-edges on the other side as outgoing, as is illustrated in Figure 2.11.

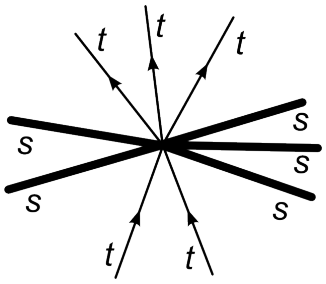

Figure 2.11: We direct the t-edges of a spiral gCDT configuration away from the initial boundary by inductively defining an ingoing and an outgoing side of a vertex using the light cone colouring condition.

Proposition 2.11. *The timelike digraph does not have any internal cycles.*

Proof. The proof that there can be no internal cycles once the digraph is defined is very similar to the proof of Proposition 2.9. □

Every vertex has a few adjacent t-edges so the timelike skeleton is a spanning graph of the entire skeleton. Note that the definition of the sides depends on the embedding of the skeleton as graph, because it depends on the order of the edges at a vertex. This is not a problem because the skeleton originates from a triangulation and therefore is endowed with a natural embedding.

Corollary 2.12. *Every directed walk can be extended to start at the initial boundary and end at the final boundary and the final boundary has only incoming t-edges at every vertex.*

Proof. The directed walks can always be extended unless they encounter a boundary, as we know from Lemma 2.8. As there are no cycles in the digraph, the configuration is finite and the walks do not return to the initial boundary, we will always encounter the final boundary if we extend a directed walk. The final boundary can per construction not contain any outgoing edges. Reversing the position of the initial and final boundary in the definition of the timelike directed graph tells us that from every vertex of the final boundary extends a reversed walk to the initial boundary. It is straightforward to see that such a walk on the reversely defined digraph is an anti-directed walk on the normal digraph. □

This also implies that the configuration is connected.

Lemma 2.13. *All spiral gCDT configurations have the topology of a cylinder.*

Proof. We already know that the configurations are connected and that their boundary is given by two circles. There are no internal topological singularities because we required a bicoloured triangulation to be a topological manifold. It might still be that there are changes in the spatial topology along the way. Again this is excluded because it would require a Morse point which is not allowed by the colouring condition, see Figure 2.12. □

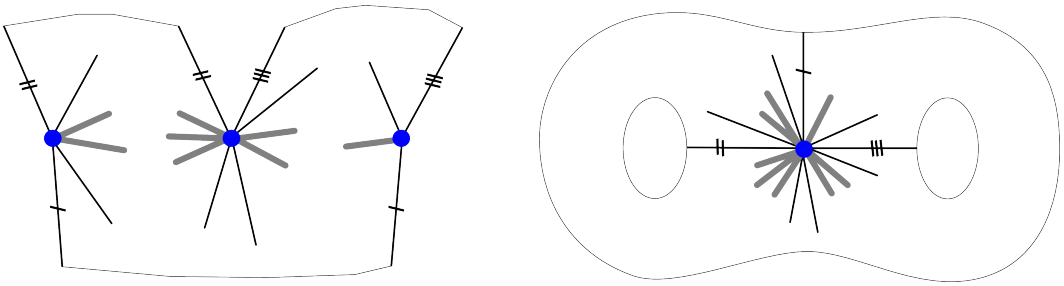

Figure 2.12: Impression of a splitting spiral gCDT configuration. Spatial topology change again requires a Morse point which is excluded by the light cone colouring condition. See also Figure 2.3.

The causal structure can now straightforwardly be defined as follows:

Definition 2.14. We say that for two vertices in a spiral gCDT configuration, *a chronologically precedes b* or $a \ll b$ if there is a non-empty directed walk, along and in the direction of the timelike digraph, from a to b.

Another interesting result concerns the exclusion of the *sss*- and *ttt*-triangles.

Theorem 2.15. *Condition 2.6(i) is superfluous: the colouring condition and the condition that the configuration is a triangulation exclude the appearance of ttt- or sss-triangles.*

Proof. The proof of Lemma 2.9 and the similar proof that excludes cycles in the entire configuration, do not make use of the *tts* and *sst* condition. If a *ttt*-triangle would appear in the configuration, then necessarily one of the edges would connect two vertices on the same side, so the definition of the timelike digraph would go awry, which is in contradiction with what has been shown above.
A similar result can be obtained for the spatial skeleton, excluding the appearance of *sss*-triangles. □

Apparently any bicoloured triangulation of a cylinder that satisfies the light cone colouring condition, will automatically exclude triangles that are coloured *sss* or *ttt*. In section 2.3 we will show that a triangle in Minkowski space whose sides have only timelike or spacelike character do not have an interpretation as a triangle with the same edge lengths in Euclidean space, so it is interesting to note that these are automatically excluded by the light cone colouring condition. All the results we have presented here also hold for the bubble gCDT and CDT configurations, which are a subclass of the spiral gCDT configurations.

2.2.5 On bubble gCDT versus spiral gCDT

It is not necessarily the case that bubble gCDT and spiral gCDT fall in the same universality class, if a continuum limit can be found for either of them at all. They are both physically

appealing generalizations of CDT and therefore it would be very interesting to know whether this is the case and also whether they behave similar to CDT.
The definition of spiral gCDT might seem much more appealing because of the locality of its conditons. But one should note that in a situation where the *sst*-triangles have a very small area and are therefore suppressed in the path sum, we expect large spirals to become very common in spiral gCDT configurations. The argument is as follows: if there are, for example, only two *sst*-triangles in a triangulation with many *tts*-triangles, then the odds are that they are relatively far apart. Because of the colouring condition, a large spiral then forms with the two *sst*-triangles at either end. Very locally a spiral might resemble a CDT configuration, but it is not precisely known what the combinatorial properties of these spirals are. At any rate we will not be able to define propagation between nice spatial hypersurfaces of which every spatial edge is a part.
In bubble gCDT on the other hand, two *sst*-triangles are not allowed to be further apart than a single strip. If the *sst*-blocks are suppressed, many bubble gCDT configurations are expected to look just like CDT configurations, but possibly with a single bubble on one particular layer. One would therefore expect that bubble gCDT reduces to CDT in this case.
In both spiral and bubble gCDT, the number of *sst*-triangles per configuration is always even, otherwise the boundary conditions cannot be met.

2.3 On Euclidean versus Lorentzian geometries

2.3.1 Colouring the triangle

We use Euclidean geometries in our path sum, but the intention is that these somehow represent the Lorentzian geometries that we would actually like to weigh. From this point of view there seems to be a logical reason why the Dynamical Triangulations approach does not deliver the right continuum behaviour in higher dimensions. A Euclidean triangle or simplex, and therefore the entire geometries in the DT path sum, do not have a unique interpretation as a Lorentzian geometry. The information that is missing is in fact precisely the information we add by colouring our triangles in CDT, as these do have a unique interpretation.

Proposition 2.16. *A Euclidean triangle with edges of length a, b and c that are coloured t, t and s respectively, can be mapped to a "tts"-triangle in two-dimensional Minkowski space, with two straight timelike edges of temporal length a and b and one straight spacelike edge of spatial length c, that is unique up to the symmetries of Minkowski space.*

We will prove an even more general result: the above holds for every three positive numbers a, b and c, not necessarily satisfying a triangle inequality.

Proof. We construct the triangle and show its uniqueness up to actions of the symmetry group of Minkowski space, which is taken to be the Poincaré group consisting of boosts and translations plus reflections in the spatial and temporal directions.

Existence We take a spatial geodesic of length c in Minkowski space. From either end point we draw the future timelike directed Minkowski sphere with radius a and b respectively, as illustrated in Figure 2.13. This is the collection of points y satisfying $\|y - x\| = r$ such that and $y - x$ is future timelike directed, for x either end of the spatial edge and $r = a, b$. The spheres have exactly one intersection point, and this can be connected to either end point of the spatial edge with straight timelike lines of length a and b.

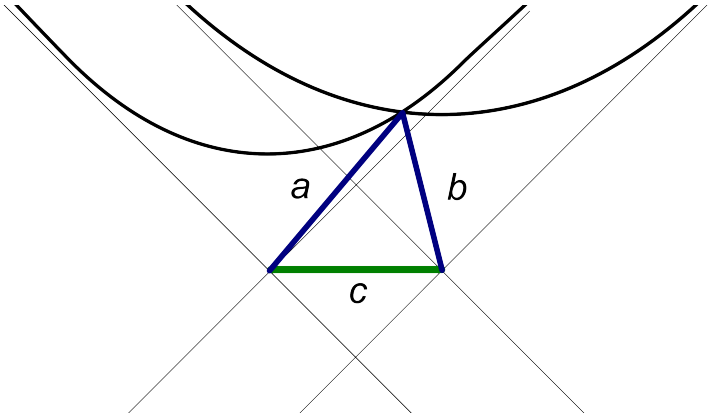

Figure 2.13: A picture illustrating the construction of the *tts*-triangle in Minkowski space with edge lengths a, b and c from Proposition 2.16.

Uniqueness The two choices for connecting the edges to the end points are related to each other by a spatial reflection. One could perform the same construction with the past timelike directed sphere and this would be related to the current construction by a temporal reflection. As the two end points of the spatial edge are spatially separated, the future directed sphere of one cannot intersect the past directed sphere of the other, so no other triangle can be created. All choices of the initial spatial edge and the resulting triangle are related to each other via boosts and translations.

□

Corollary 2.17. *The equivalent statement holds for the sst-coloured Euclidean triangle.*

Proof. This follows from Proposition 2.16 by the space and time symmetry of two-dimensional Minkowski space. □

Another interesting result is the following.

Proposition 2.18. *A Euclidean triangle can never be mapped to a "ttt"-triangle in two-dimensional Minkowski space with three timelike edges, such that the timelike length of these edges equals the edge lengths of the Euclidean triangle.*

Proof. For Euclidean triangles with edges a, b, c holds the Euclidean triangle inequality:

$$a \leq b + c, \tag{12}$$

and all permutations thereof. For a triangle of three timelike geodesics in Minkowski space however, there is one edge whose proper time is longer than that of the other two combined, so a reversed triangle inequality holds:

$$a \geq b + c. \tag{13}$$

This is the origin of the twin paradox in Minkowski space. The two inequalities can only hold simultaneously in the case of equality, in which case the lines are parallel and there is no triangle. □

Corollary 2.19. *The same holds for the "sss"-triangle.*

Proof. Again this follows from Proposition 2.18 by space and time symmetry. □

Similar results hold in higher dimensions.

2.3.2 The geometry of the triangles in CDT and gCDT

Because we want our triangulation to fit together nicely, we choose only two edge lengths in CDT and generalized CDT, one spatial a_s and one temporal a_t. In Minkowski space the usual triangle inequalities do not hold and the ratio of these two edge lengths can vary between zero and infinity, while still being able to form a nice *tts*- or *sst*-triangle. However, for the triangle to have an interpretation as a Euclidean triangle, the edges need to satisfy the triangle inequality. In order to be able form both the *tts*- and *sst*-triangle in Euclidean space we should therefore require

$$\frac{1}{2} \leq \frac{a_t}{a_s} \leq 2. \tag{14}$$

This parameter is irrelevant for CDT as we only have the freedom to choose the area of the *tts*-triangle. For gCDT it does become important, because this ratio determines the relative areas of the *tts*- and *sst*-triangles and with that their respective weights.

3 Strip Propagator Approach

3.1 Solving a discrete model

By "solving" a model in a quantum theory, one usually means determining the spectrum of eigenvalues of the Hamiltonian operator $\hat{H}$ and the associated eigenstates. In order to come anywhere near this formulation and such a solution, starting from a discretized gravitational path integral, one should first determine the behaviour of the discretized model, derive the limiting continuum behaviour amd then study the resulting effective continuum theory. In this thesis we will only concern ourselves with the study of the discrete path sum. This in the first place comes down to partitioning the sets of discrete geometries in a way that allows us to get a grip on the number of geometries. We then concretely perform the path sum or a similar sum and determine its behaviour as a function of the coupling constants. More steps are needed to obtain an effective continuum theory and an idea of the physics generated by the model.

3.2 For CDT

The most straightforward way to solve the two-dimensional path integral of CDT is via the method of transfer matrices or strip propagators, as presented in [13]. In this approach we compute the Euclidean partition sum by partitioning the CDT triangulations into subsets with an equal number of strips k. We then describe propagation over k strips in terms of the propagator for one strip G_s. The behaviour of the path sum and its continuum limit can then be determined.
In this section we consider the discrete path sum in an approach that is derived from the partinioning into strips. It differs in terms of computation from [13], but is similar to the approach taken by Durhuus et al. in [25].
We will sometimes refer to a spatial layer with a certain number of vertices a as the *state* a.

3.2.1 Partitioning

We consider the CDT path sum without fixed boundaries, so summing over all possible boundary conditions. Neglecting prefactors, the grand-canonical sum we want to study is the following:

$$Z_{CDT} \propto \sum_{T\in\mathcal{T}} \frac{1}{C_T}\, g^{N(T)} = \sum_{a,b=1}^{\infty} G(a,b), \tag{15}$$

where $N(T)$ counts the number of triangles in a triangulation, $g = e^{-\lambda A_{tts}}$ is the weight of a single triangle and $\mathcal{T}$ is the set of all CDT triangulations of any size. C_T is the order of the symmetry group of T. We work with a preferred time direction, so the only symmetries we are dealing with here are discrete rotations that leave the triangulation invariant. The last term defines the *propagator*[2] $G(a,b)$ between initial and final states a and b respectively[3]. This is the amplitude for given boundary conditions of the geometries, which are summed over to form the entire path sum.
Let $\{S_k\}_{k\geq 1}$ be the partition of $\mathcal{T}$ into triangulations with k strips and $k-1$ intermediate virtual states. Note that $N(T)$ does not factorize over this partition because there can be any number of vertices on the intermediate circles. We can subdivide S_k into classes $S_{(a_i)}$ that have the same ordered set of intermediate states $(a_i)_{i=0}^{k}$. By this we mean that

[2] This is not what one usually calls a propagator, which is a quantity with a fixed time interval, while $G(a,b)$ is the amplitude of all configurations with boundaries a and b.
[3] Many papers use the reversed notation, i.e. $G(b,a)$ with a the initial state and b the final state.

the i^{th} spatial layer has $a_i \in \mathbb{N}_{\geq 1}$ vertices, where the initial and final state are labelled 0 and k respectively. Every class of triangulations $S_{(a_i)}$ has the same number of vertices and therefore the same number of triangles, so the volume function does factorize over this subpartition. We have:

$$\begin{aligned} Z_{CDT} &\propto \sum_{\{S_k\}} \sum_{\{S_{(a_i)}\}} \sum_{T \in S_{(a_i)}} \frac{1}{C_T}\, g^{N(T)} && (16)\\ &= \sum_{k=1}^{\infty} \sum_{a_0,\ldots,a_k=1}^{\infty} \left(\sum_{T \in S_{(a_i)}} \frac{1}{C_T} \right) g^{N((a_i))} && (17)\\ &\equiv \sum_{k} \sum_{a_0,a_k} G(a_0, a_k; k). && (18) \end{aligned}$$

In the last line we have defined the k-strip propagator $G(a, b; k)$, which is the amplitude in the partition sum for propagating from state a to state b with k intermediate strips.

3.2.2 The path sum in terms of one-strip propagators

The k-strip propagator satisfies the following rule:

Claim 3.1. *We have:*

$$\begin{aligned} G(a, b; k) &= \sum_{T \in S_k(a,b)} \frac{1}{C_T}\, g^{N(T)} && (19)\\ &= \sum_{l} \sum_{T_1 \in S_1(a,l)} \sum_{T_2 \in S_{k-1}(l,b)} \left(\frac{1}{C_{T_1}}\, l\, \frac{1}{C_{T_2}} \right) g^{N(T_1)+N(T_2)} && (20)\\ &= \sum_{l} G_s(a, l)\, l\, G(l, b; k-1), && (21) \end{aligned}$$

where we define the one-strip propagator $G_s(a, l) = G(a, l; 1)$ and $S_k(a, b) \subset S_k$ is the subset of triangulations with k strips and fixed boundary states a and b.

Proof. We separate three cases: T_1 and T_2 both do not have any symmetry (I), only one of the two has some symmetry (II) or they both have a non-trivial symmetry (III).

(I) If T_1 and T_2 both do not have any symmetry, so $C_{T_1} = C_{T_2} = 1$, then there are l ways to combine the two to form different elements of $S_k(a, b)$ and $C_T = 1$. Indeed

$$\frac{1}{C_{T_1}}\, l\, \frac{1}{C_{T_2}} = l. \tag{22}$$

(II) If one of the two configurations, say T_i, has some symmetry, say $C_{T_i} = m$, which has to be a divisor of l, then the number of distinct configurations one can create from T_1 and T_2 by gluing them along the state l is l/m. The union T of the two configurations does not have any symmetry anymore. Indeed we have

$$\frac{1}{C_{T_1}}\, l\, \frac{1}{C_{T_2}} = \frac{l}{m}. \tag{23}$$

(III) Suppose both T_1 and T_2 exhibit symmetry, say $C_{T_1} = m$ and $C_{T_2} = n$ and let $c = \gcd(m, n)$. The situation can be represented by the following diagram:

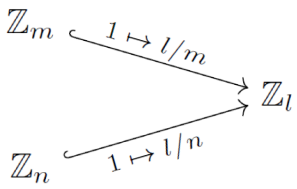

Here $\mathbb{Z}_m$ and $\mathbb{Z}_n$ are the symmetry groups of T_1 and T_2 and they are embedded in the group $\mathbb{Z}_l$ of relative rotations of the two configurations. The patterns on T_1 and T_2 repeat themselves every l/m and l/n vertices respectively. The symmetry group of the glued triangulation is given by the intersection of the images of $\mathbb{Z}_m$ and $\mathbb{Z}_n$ in $\mathbb{Z}_l$ under the above maps, which is the image of $\mathbb{Z}_c$ under the embedding:

$$\mathbb{Z}_c \xhookrightarrow{1 \mapsto l/c} \mathbb{Z}_l$$

so we have that the order of the symmetry group of the glued configuration C_T equals c.

To discover the number of inequivalent triangulations, we cyclically label the different gluings of the two configurations with an element of $\mathbb{Z}_l$ (so 1 to l), where adding 1 to the label corresponds to rotating the two configurations relative to each other by one edge, in a chosen direction. Two gluings x and $\tilde{x}$ are equivalent due to the symmetries of the two configurations if

$$r = x - \tilde{x} = q\frac{l}{m} + q'\frac{l}{n}, \tag{24}$$

for two integers q and q'. The periodicity of the gluing, which is the smallest difference for which the patterns repeats itself, is the smallest number r for which (24) holds. By Bézout's lemma this is equal to

$$r = \gcd(\frac{l}{m}, \frac{l}{n}). \tag{25}$$

To calculate r, we realize that $m|l$, $n|l$ and $c|l$, and we can thus write

$$l = p \cdot \frac{m}{c} \cdot \frac{n}{c} \cdot c, \tag{26}$$

where $\frac{m}{c}$ and $\frac{n}{c}$ are coprime and $p \in \mathbb{N}$. Therefore

$$r = \gcd(p\frac{n}{c}, p\frac{m}{c}) = p = \frac{l\,c}{m\,n}. \tag{27}$$

So indeed we now have

$$\frac{r}{C_T} = \frac{l\,c}{m\,n}\frac{1}{c} = \frac{l}{m\,n} = \frac{1}{C_{T_1}}\,l\,\frac{1}{C_{T_2}}. \tag{28}$$

□

Corollary 3.2. *By induction we obtain from 3.1 that we can write our k-strip propagator entirely in terms of one-strip propagators:*

$$\begin{aligned} G(a_0, a_k; k) &= \sum_{a_1,\ldots,a_{k-1}} \left(\sum_{T_1 \in S_1(a_0,a_1)} \frac{1}{C_{T_1}} \right) a_1 \ldots \\ &\qquad \ldots a_{k-1} \left(\sum_{T_k \in S_1(a_{k-1},a_k)} \frac{1}{C_{T_k}} \right) g^{\sum_i N(T_i)} \\ &= \sum_{a_1,\ldots,a_{k-1}} G_s(a_0, a_1)\, a_1 \ldots a_{k-1} G_s(a_{k-1}, a_k) \end{aligned} \tag{29}$$

This result is represented pictorially in Figure 3.1.

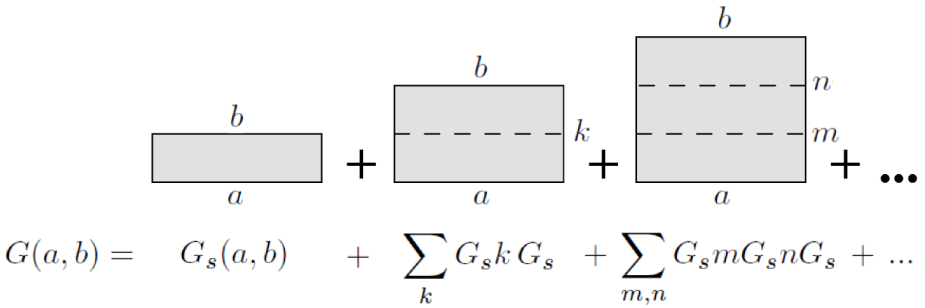

Figure 3.1: A pictorial representation of the strip propagator approach to partitioning the set of CDT triangulations $\mathcal{T}$: propagation along any number of strips $G(a, b)$ is propagation along k strips summed over k.

3.2.3 The one-strip propagator

We have expressed our partition sum in terms of one-strip propagators. In order to solve it, we should take a closer look at the one-strip propagator $G_s(a, b)$ itself. We have

$$G_s(a, b) = \left(\sum_{T \in S_1(a,b)} \frac{1}{C_T} \right) g^{a+b} \equiv \mathcal{N}(a, b) g^{a+b}. \tag{30}$$

Claim 3.3.

$$\mathcal{N}(a, b) \equiv \sum_{T \in S_1(a,b)} \frac{1}{C_T} = \frac{(a + b - 1)!}{a!b!} = \frac{1}{a} \binom{a + b - 1}{a - 1} \tag{31}$$

Proof. First we mark one vertex on the starting ring with a vertices.

Every configuration has a rightmost edge connecting the marked vertex with an element of the ring with b vertices. We cut the strip along this edge. There are $a + b$ edges inside the strip, so subtracting the cutting edge, there are $a + b - 1$ edges to distribute into a triangulation.

For all b vertices on the upper ring we choose the rightmost edge that connects to it. This completely determines the rest of the configuration. See also Figure 3.2.

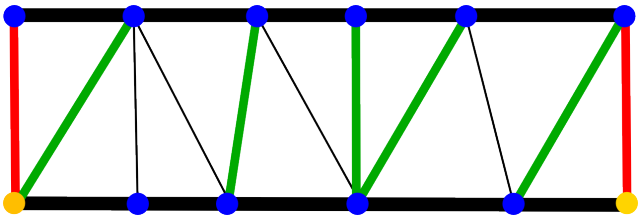

Figure 3.2: Example of a strip with $a = 5$ and $b = 5$. We have marked a vertex on the initial ring (yellow) and cut along its rightmost edge (red). We then choose the rightmost edges for every one of the upper vertices (green) and this determines the configuration because it should be a triangulation. This amounts to choosing b out of the remaining $a + b - 1$ edges.

We therefore have $\binom{a+b-1}{b}$ different strips with a marked vertex. For an unmarked strip without symmetry, there are a marked strips corresponding to it, so we should divide the number by a. If an unmarked strip does have symmetry, say the order of the symmetry group is C, then there are a/C marked strips corresponding to it. This sums precisely to formula (31).

□

3.2.4 Computing the partition sum

We can now rewrite our partition sum as follows:

$$\begin{aligned} Z &= \sum_{k=1}^{\infty} \sum_{a_0 \dots a_k} g^{a_0} \mathcal{N}(a_0, a_1) g^{2a_1} a_1 \mathcal{N}(a_1, a_2) \dots g^{2a_{k-1}} a_{k-1} \mathcal{N}(a_{k-1}, a_k) g^{a_k} \\ &= \sum_{k=1}^{\infty} A_k(g) \qquad (32) \\ &= \sum_{k=1}^{\infty} \sum_{a_k=1}^{\infty} \tilde{A}_k(a_k, g), \qquad (33) \end{aligned}$$

where the functions $\tilde{A}_k$ can be related to each other via the following formula:

$$\tilde{A}_k = \sum_{a_{k-1}} \tilde{A}_{k-1} \cdot a_{k-1} g^{a_{k-1}} \mathcal{N}(a_{k-1}, a_k) g^{a_k}. \qquad (34)$$

Claim 3.4. *We have*

$$\tilde{A}_k(a_k, g) = \frac{g^{a_k}}{a_k} \left(-B_k^{a_k} + C_k^{a_k} \right), \qquad (35)$$

where $B_k = f(B_{k-1})$, $C_k = f(C_{k-1})$ *with* $f(x) = \frac{1}{1-g^2 x}$, $B_1 = 1$ *and* $C_1 = \frac{1}{1-g}$.

Proof. We prove the claim by induction.

Induction basis

$$\begin{aligned}\tilde{A}_1 &= \sum_{a_0} g^{a_0}\mathcal{N}(a_0,a_1)g^{a_1} \\ &= \frac{g^{a_1}}{a_1}\sum_{a_0=1}^{\infty} g^{a_0}\binom{a_0+a_1-1}{a_1-1} \\ &= \frac{g^{a_1}}{a_1}\left(-1+\frac{1}{(1-g)^{a_1}}\right) \\ &= \frac{g^{a_1}}{a_1}\left(-B_1^{a_1}+C_1^{a_1}\right) \end{aligned} \tag{36}$$

Where we have used the identity:

$$\sum_{n=0}^{\infty}\binom{n+k-1}{n}z^n = \frac{1}{(1-z)^k} \tag{37}$$

Induction step We assume $\tilde{A}_k$ is of the form (35).

$$\begin{aligned}\tilde{A}_{k+1} &= \sum_{a_k}\frac{g^{a_k}}{a_k}\left(-B_k^{a_k}+C_k^{a_k}\right)g^{a_k}a_k\mathcal{N}(a_k,a_{k+1})g^{a_{k+1}} \\ &= \frac{g^{a_{k+1}}}{a_{k+1}}\sum_{a_k}\left(-(g^2B_k)^{a_k}+(g^2C_k)^{a_k}\right)\binom{a_k+a_{k+1}-1}{a_{k+1}-1} \\ &= \frac{g^{a_{k+1}}}{a_{k+1}}\left(-\frac{1}{(1-g^2B_{k+1})^{a_{k+1}}}+\frac{1}{(1-g^2C_{k+1})^{a_{k+1}}}\right) \\ &= \frac{g^{a_{k+1}}}{a_{k+1}}\left(-B_{k+1}^{a_{k+1}}+C_{k+1}^{a_{k+1}}\right) \end{aligned} \tag{38}$$

□

We perform the sum over a_k of the functions $\tilde{A}_k$ to obtain the functions $A_k(g)$ that were defined in (32). Note that $A_k = \sum_{a,b} G(a,b;k)$ and might be viewed as the k-strip propagator without fixed boundary conditions.

$$\begin{aligned}A_k &= \sum_{a_k=1}^{\infty}\frac{g^{a_k}}{a_k}\left(-B_k^{a_k}+C_k^{a_k}\right) \\ &= \log\left(\frac{1-gB_k}{1-gC_k}\right) \end{aligned} \tag{39}$$

For the path sum as we have defined it we can then write:

$$Z(g)_{CDT} \propto \sum_{k=1}^{\infty}A_k(g) = \sum_{k=1}^{\infty}\log\left(\frac{1-gB_k(g)}{1-gC_k(g)}\right). \tag{40}$$

3.2.5 Critical behaviour of the model

The limiting behaviour of the model now depends on the limiting behaviour of $A_k(g)$ as the number of strips $k \to \infty$. We have

$$\lim_{k\to\infty} A_k(g) = \lim_{k\to\infty} \log\left(\frac{1-gB_k(g)}{1-gC_k(g)}\right) \tag{41}$$

so this behaviour is directly related to the limits of the two iterations.
The two iteratively defined functions B_k and C_k are both iterations of $f(x) = (1-g^2x)^{-1}$. For different values of g, the functions B_k and C_k will behave differently. In some cases they have a well-defined limit and we define

$$B(g) = \lim_{k\to\infty} B_k(g) \tag{42}$$

$$C(g) = \lim_{k\to\infty} C_k(g). \tag{43}$$

Note that if $B \neq C$, then A_k converges to a constant, while if $B = C$, A_k converges to 0. For $g > 1/2$, $f(x)$ does not have a fixed point and the values of B_k and C_k will vary chaotically. In the case $g < 1/2$, f has two fixed points, but both functions will converge to the lowest one. If $g = 1/2$, $f(x)$ has precisely one fixed point, and this turns out to be the critical point in the phase diagram. The next step is to study the continuum behaviour and the expectation value of observables. This can be found in [13].

3.3 Constructing a similar approach for bubble gCDT

3.3.1 A similar partitioning for bubble gCDT

If we consider the configurations of bubble gCDT, we will soon notice that a similar partition of shapes as we have seen in the strip propagator approach is also possible for bubble gCDT. Instead of only the strips, the triangulations can now be thought of as consisting of two macroscopic shapes, namely strips and bubbles. The strips can be thought of as gaps in the spatial skeleton of the configurations. A piece of the configuration between two strips, whose spatial skeleton is a connected component of the entire spatial skeleton, we call a *bubble complex*.
The grand canonical path sum of bubble gCDT can be described as follows.

$$Z_{gCDT} \propto \sum_{T\in\mathcal{T}} \frac{1}{C_T}\, g^{N_0(T)}\, \tilde{g}^{N_1(T)} = \sum_{a,b=1}^{\infty} G(a,b), \tag{44}$$

where now $\mathcal{T}$ stands for all bubble gCDT configurations, N_0 is the number of tts-triangles of a configuration, whose weight is $g = e^{-\lambda A_{tts}}$ and N_1 is the number of sst-triangles, whose weight is $\tilde{g} = e^{-\lambda A_{sst}}$. The functional can again be split up in "propagators" $G(a,b)$ because we know that both boundaries are given by spatial circles with a certain unconstrained number of vertices a and b.
The proof of Claim 3.1 does not depend on T_1 and T_2 being strips, and can therefore straightforwardly be generalized to the case where one of the two is a bubble complex and the other a strip. We can therefore again split up our symmetry factors and construct a similar approach as in the previous section. In generalization of the strip partitioning as it was laid out in Figure 3.1, we can now make a partitioning of the configurations into strips and bubble complexes as illustrated in Figure 3.3. In order to do this, we should define the minimal bubble complex to be one without bubbles, so just a single spatial circle, such that a CDT configuration can be thought of as a bubble gCDT configuration with zero bubbles for every bubble complex. In that case however, we see that the minimal bubble gCDT configuration in the first term of Figure 3.3 is also a single spatial circle, which does not have the topology of a cylinder. This is why these configurations were included in the definition of bubble gCDT in subsection 2.2.3.

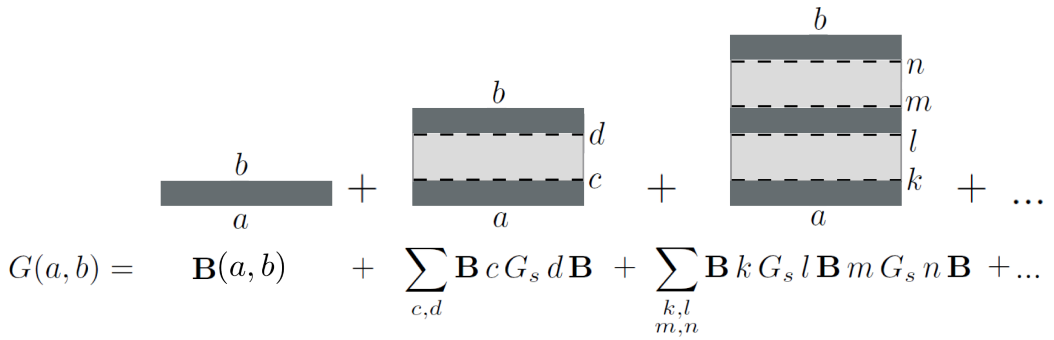

Figure 3.3: A pictorial representation of the generalized strip propagator approach for bubble gCDT. The bubble gCDT propagator can be thought of as a sum over n of the amplitude of configurations with n intermediate strips. Between those strips and on either end there can also be any bubble complex, whose propagator we call $\mathbf{B}$. In the picture the bubble complexes are coloured dark and the strips light.

We again write the propagator $G(a, b)$ in terms of n-strip propagators, where now between and on either side of the n strips there is the more complicated structure of a bubble complex.

$$G(a,b) = \sum_{n=0}^{\infty} G(a,b;n) \tag{45}$$

$$G(a_0,b_n;n) = \sum_{\substack{a_1,\ldots,a_n \\ b_0\ldots b_{n-1} \\ =1}}^{\infty} \mathbf{B}(a_0,b_0)b_0 G_s(b_0,a_1)a_1 \ldots b_{n-1}G_s(b_{n-1},a_n)a_n\mathbf{B}(a_n,b_n) \tag{46}$$

The strip propagator G_s was calculated in the previous section. The question now is what the bubble complex propagator $\mathbf{B}(a, b)$ should be. Every bubble complex consists of a stacking of a certain number k of bubbles. It is therefore evident that the bubble complex propagator should sum all these possibilities with their appropriate weights:

$$\mathbf{B}(a,b) = \sum_{k=0}^{\infty} B_k(a,b). \tag{47}$$

The amplitude $B_k(a, b)$ we call the k-bubble propagator.

3.3.2 Iterative model

It would be very nice if we could exactly generate all configurations by adding one bubble at a time *iteratively*, irrespective of the position of the previous ones, such that the following simple formula would hold for the k-bubble propagators.

$$B_k(a,b) = \text{“}B_1^k\text{”} = \sum_{l_1,..l_{k-1}} B_1(a,l_1)B_1(l_1,l_2)...B_1(l_{k-1},b) \tag{48}$$

This would imply that the one-bubble propagator B_1 could be viewed as a self-energy term of the CDT layer, and we could formulate a *Dyson equation* for the bubble complex propagator, as illustrated in Figure 3.4. We call this approach the iterative model.

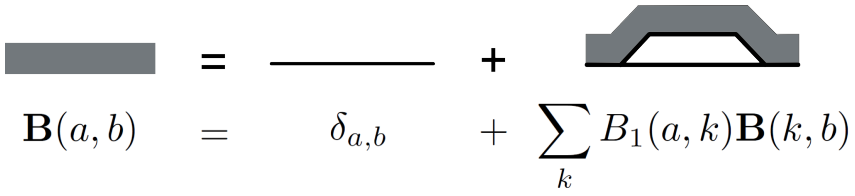

Figure 3.4: A Dyson equation formulates that the one-bubble propagator is viewed as a self-energy of a spatial CDT layer.

Unfortunately the iterative method does not give us the right set of configurations, as is illustrated in Figure 3.5. If two bubbles are added next to each other, then the order of adding the two bubbles does not matter and we obtain the same configuration for both ways of ordering. If the bubbles are added on top of each other, then two different configurations can appear, depending on the order of the bubbles. This method therefore does not generate every configuration exactly once, but some of them are overcounted.

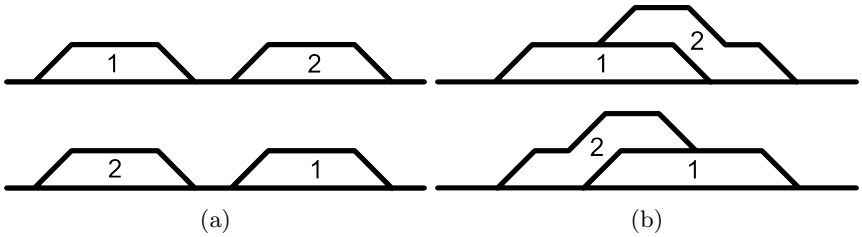

Figure 3.5: When we glue two bubbles on a spatial layer one by one, the order, here indicated by the number inside the bubble, does not matter if the bubbles are placed beside each other as in (a), but does matter if the second bubble is placed on top of the first as in (b). This is why the iterative addition of bubbles does not generate every configuration exactly once.

It is interesting to note that the configurations that are overcounted are precisely the ones for which there is no unique definition of bubble time. The iterative approach generates all configurations as if the bubbles were *labelled*. Even though the iterative or labelled approach does not have a one-to-one correspondence with bubble gCDT, the model might still be interesting to study. There is a chance that it actually ends up in the same universality class as bubble gCDT, although one should of course then also find a proof of this. In section 3.5 we study the model in more detail and also compute the one-bubble propagator B_1 and start the computation of the two-bubble propagator of normal bubble gCDT by compensating for the overcounting of the iterative model.

3.3.3 Characterizing topologies

The k-bubble propagator cannot be considered simply as the addition of k independent bubbles, so instead of treating the bubbles as independent objects within a bubble complex, we will have to classify the possible configurations of stackings of k bubbles. A convenient way of treating the bubble complexes is to look at the topological structure of the spatial skeleton, where we forget about the two-valent vertices of this graph. This is illustrated in Figure 3.6. We will call this the *topological graph* of a bubble complex, and we will call the set of possible topological graphs of a k-bubble complex $\mathcal{T}_k$. We do keep track of the

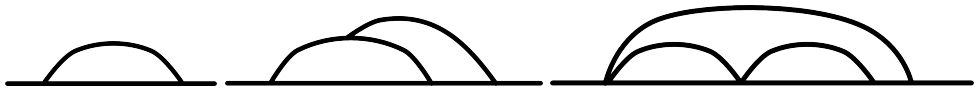

(a) (b) (c)

Figure 3.6: Three topological graphs of bubble complexes. Graph (a) is one of the two elements of $\mathcal{T}_1$, (b) is an element of $\mathcal{T}_2$ and (c) is in $\mathcal{T}_3$.

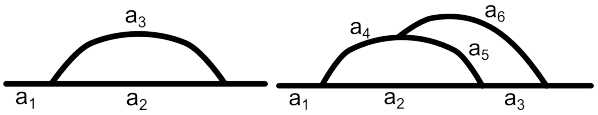

(a) (b)

Figure 3.7: The line elements of two topological graphs.

embedding of the graph in the cylinder, i.e. we know "which way around" every line runs. This is necessary because the two different choices for a line to go around the cylinder give rise to intrinsically different bubble complexes. We will also assume that this information is available for a spatial skeleton.
In the topological graphs, we call the pieces of line between the (three- or higher-valent) vertices *line elements*. For a given topological graph, we label the line elements $1, \ldots, n(T)$, where $n(T)$ is the number of line elements of the graph. In a realization of a topological graph as a bubble complex, every line element i will be endowed with a certain number of two-valent vertices a_i. If for every line element in a topological graph we have defined the number of two-valent vertices, then we are back to a spatial skeleton, as in Figure 3.7.
For every topological graph, we can add any number of vertices greater or equal to one, to any of the line elements, and the resulting spatial skeleton will still have a realization as a bubble complex. So in this description the lengths of the line elements become unconstrained parameters over which we can sum freely in the computation of the bubble propagator. This is expressed by the following formula:

$$B_k(a,b) = \sum_{T\in\mathcal{T}_k} \sum_{\substack{a_1,\ldots \\ a_{n(T)}=1}}^{\infty} \mathcal{A}_T(a_1 \ldots a_{n(T)}) g^{N_0(T,a_1,\ldots,a_{n(T)})} \tilde{g}^{2k}, \tag{49}$$

with

$$\mathcal{A}_T(a_1 \ldots a_{n(T)}) = \sum_{\substack{B\in \\ S_{T,a_1\ldots a_{n(T)}}}} \frac{1}{C_B}, \tag{50}$$

where $S_{T,a_1\ldots a_{n(T)}}$ is the set of distinct bubble complexes with a spatial skeleton of the topological graph T with line element lengths $a_1, \ldots, a_{n(T)}$, with $n(T)$ the number of line elements of the topological graph T. $\mathcal{A}_T$ is the combinatorial factor that stems from decorating the spatial skeleton with timelike edges. The number of tts-triangles N_0 is completely determined by the spatial skeleton. The number of sst-triangles is always $2k$ for a complex with k bubbles.
We define a_i to be the length or the number of spatially two-valent vertices on the line element i. If $a_i = 0$, then the length of element i is a single spacelike edge. This is possible for some of the lines, but not for others. For example, in Figure 3.7b, the labels a_1, a_3, a_4

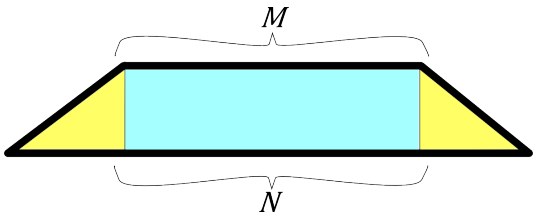

Figure 3.8: Illustration of how the vertices covered by the bubble (N) and on top of the bubble (M) are defined.

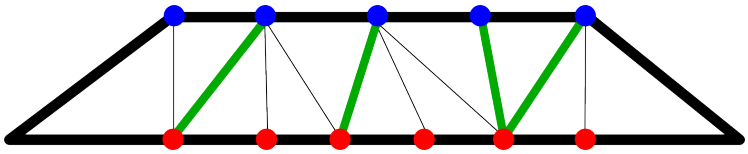

Figure 3.9: Example of a bubble with $M = 5$ (blue) and $N = 6$ (red). From left to right we choose the first edges that connect to each upper vertex and this completely determines the configuration. The first one is already determined.

and a_5 are allowed to take value zero, but a_2 and a_6 are not, because a bubble consists of at least two *sst*-triangles. For simplicity we will write that the a_i run from 1 to ∞. Which line elements are allowed to have length zero is well-defined for the topological graph and does not depend on the lengths of the other line elements.
The topological graphs are not degenerate, i.e. two different topological graphs cannot give rise to the same configuration by choosing the lengths of the line elements in a certain way.

3.3.4 Decorating a bubble

We will investigate the amplitude $\mathcal{A}_T$ of decorating a spatial skeleton with timelike edges in a bit more detail in the next few subsections. From this point on we will neglect the symmetry factor of the entire bubble complex C_B in (50). The bubbles themselves do not have any internal cyclic symmetry because they have two ends. First we will discuss the decoration of a single bubble with timelike edges.

Claim 3.5. *There are $\mathcal{M}(M,N)$ ways to decorate the spatial skeleton of a single bubble with timelike edges, with M the number of vertices on top of the bubble and N the number of vertices covered by the bubble as illustrated in Figure 3.8, with*

$$\mathcal{M}(M,N) = \binom{M+N-2}{M-1} = \frac{(M+N-2)!}{(M-1)!\,(N-1)!}. \tag{51}$$

Proof. As there is now a beginning and an end vertex, we do not have to deal with marking and unmarking. There are $M+N-1$ timelike edges inside the bubble. From left to right, we choose the rightmost edges of every upper vertex and this completely determines the rest of the configuration, as illustrated in Figure 3.9. The first one is already chosen for us, so we are left with $M-1$ choices out of a set of $M+N-2$. □

3.3.5 Partitions of line elements

We consider a spatial skeleton with topological graph $T \in \mathcal{T}_k$ and line elements $a_1, \ldots, a_{n(T)}$, with $n(T)$ the number of line elements of the topological graph. We have

$$k - 1 \leq n(T) \leq 3k. \tag{52}$$

The number of line elements is at most three times the number of bubbles, because every bubble can maximally divide a line in three pieces, see also section 3.4. The minimal number of line elements occurs if all vertices of the topological graph coincide.
Consider the set $\{1, \ldots, n(T)\}$ of fixed labels for the line elements of T. Every line element either appears once on the bottom of a bubble or it is on top of the bubble complex. At the same time every line element appears once on top of a bubble, or is on the bottom of the bubble complex. We choose a labelling of the bubbles in T from 1 to k. We can define two partitions of the set of line elements labels $\{i\}_{i=1}^{n(T)}$.

Definition 3.6. The bottom partition x_j
We define x_j for $j = 1, \ldots, (k+1)$ to be a partition of the line element labels $\{i\}_{i=1}^{n(T)}$, such that x_j, $j = 1, \ldots, k$ consists of the line elements at the bottom of the j^{th} bubble and x_{k+1} consists of the line elements on top of the bubble configuration.

Definition 3.7. The top partition y_j
We define y_j for $i = 0, \ldots, k$ to be a partition of the line element labels $\{i\}_{i=1}^{n(T)}$, such that y_0 consists of the line elements on the bottom of the bubble configuration and y_j, $j = 1, \ldots, k$ consists of the line elements on top of the j^{th} bubble.

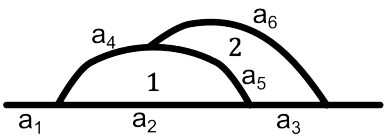

j	0	1	2	3
x_j		$\{2\}$	$\{3,5\}$	$\{1,4,6\}$
y_j	$\{1,2,3\}$	$\{4,5\}$	$\{6\}$	

Figure 3.10: Example of the bottom and top partitions of a topological graph.

Figure 3.10 gives an example of the partitions x_j and y_j for a given topological graph in $\mathcal{T}_2$ with a certain labelling (1 and 2) of the bubbles and (1 to 6) of the line elements. There are a few things one can say about these two partitions. In the first place, they are partitions, so we have

$$\bigcup_{j=1}^{k+1} x_j = \bigcup_{j=0}^{k} y_j = \{1, \ldots, n(T)\}. \tag{53}$$

Furthermore we have that the j^{th} bubble has the line elements x_j at the bottom and y_j on top. We have

$$x_j \cap y_j = \emptyset \tag{54}$$

The number of vertices on either side of a bubble is the added line element lengths plus the intermediate vertices between the line elements, which are vertices of the topological graph. Let N_j be the number of vertices covered by bubble j and M_j the number of vertices on

top of the bubble j. We have

$$N_j = \sum_{i\in x_j} a_i + |x_j| - 1 \tag{55}$$

$$M_j = \sum_{i\in y_j} a_i + |y_j| - 1. \tag{56}$$

For a bubble with M, N vertices, the number of tts-triangles is $M + N - 2$, so the number of tts-triangles in the bubble j is:

$$N_0(j) = N_j + M_j - 2 = \sum_{i\in x_j} a_i + \sum_{i\in y_j} a_i + |x_j| + |y_j| - 4. \tag{57}$$

We see that to obtain the minimal size of the bubble, so $N_0(j) = 0$, we still need to have $M_j = N_j = 1$ as there are two sst-triangles inside the bubble. This can be realized either because there is an intermediate vertex between two line elements on top or below the bubble or because the length of the line element is 1. This is why some line elements are not allowed to have zero vertices.
If the labelling of the bubbles in T is compatible with a definition of bubble time on the bubble complex, then we can furthermore say that

$$|x_1| = |y_k| = 1 \tag{58}$$

$$x_j \subset \bigcup_{i=0}^{j-1} y_i \tag{59}$$

$$1 \leq |y_0|, |x_{k+1}| \leq 2k. \tag{60}$$

3.3.6 The bubble propagator amplitude

With the knowledge and definitions from the previous subsections, we can now write for the amplitude of a spatial skeleton with topological graph T and line element lengths $\{a_i\}$:

$$\begin{aligned}\mathcal{A}_T(\{a_i\})g^{N_0}\tilde{g}^2 k &= \prod_{j=1}^{k} \mathcal{M}(M_j, N_j) g^{M_j+N_j-2}\tilde{g}^2 \\ &= \tilde{g}^{2k} g^{2\sum_{i=1}^{n(T)} a_i + 2n(T) - 4k - V_{y_0} - V_{x_{k+1}}} \\ &\qquad \prod_{j=1}^{k} \mathcal{M}(\sum_{i\in y_j} a_i + |y_j| - 1, \sum_{i\in x_j} a_i + |x_j| - 1).\end{aligned} \tag{61}$$

The expressions V_{y_0} and $V_{x_{k+1}}$ stand for the vertices on the bottom and the top of the bubble complex respectively, for which holds

$$V_{y_0} = \sum_{i\in y_0} a_i - |y_0| = a_m \tag{62}$$

$$V_{x_{k+1}} = \sum_{i\in x_{k+1}} a_i - |x_{k+1}| = b_m, \tag{63}$$

where the a_m and b_m refer back to equation (46), if the bubble complex is in position m. Note that the term $g^{b_m+a_{m+1}}$ appears in G_s in (46), so these terms in (61) will be cancelled in the final expression.

Obtaining an expression for the bubble complex propagator and, via this, an expression for the entire bubble gCDT propagator, now only depends on finding a classification of the topological graphs together with the information that is contained in the bottom and top partitions x_j and y_j. These classification problems are in general not straightforward to solve. In the next section we will simplify the problem somewhat to obtain an insight into the structure of the sets of topological graphs.

3.4 Restricting to two or three valence in the spatial skeleton

In this section we will simplify the problem of classifying the possible topological graphs somewhat by restricting the set of allowed configurations such that the spatial valence of the vertices equals two or three. This means that at every vertex, maximally one bubble is allowed to either begin or end. This simplification has the advantage that the number of line elements $n(T)$ is always precisely equal to its maximal value of $3k$. We give a graphical overview of the elements of $\mathcal{T}_k$ with this restriction.

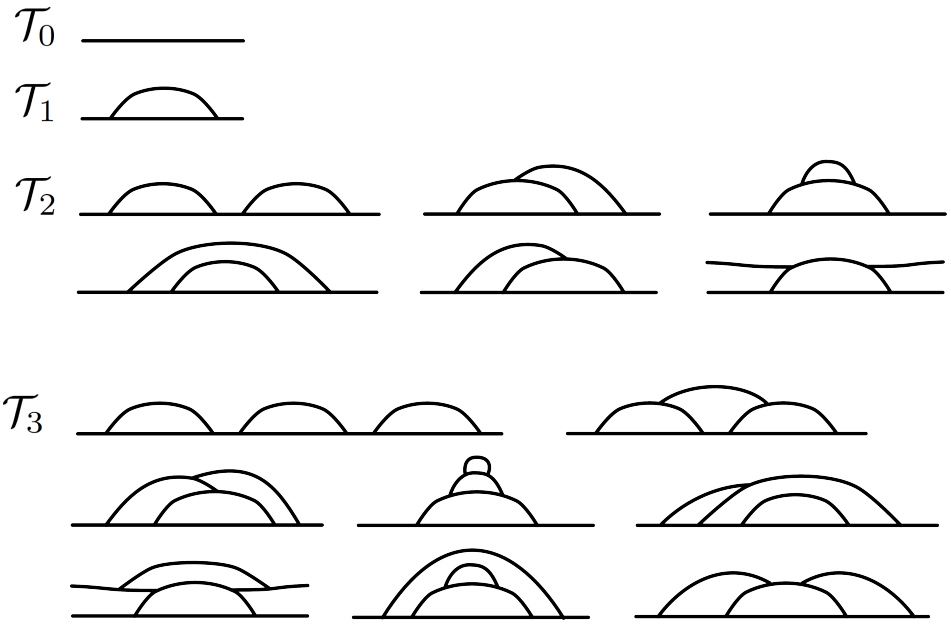

We present only a few topological graphs of $\mathcal{T}_3$, which has 57 elements. The elements of $\mathcal{T}_k$ can be generated iteratively by considering every element of $\mathcal{T}_{k-1}$ and connecting the line elements that are on top of the configuration to each other both ways around the cylinder. If an element A of $\mathcal{T}_{k-1}$ has $n = |x_k|$ line elements on top of the configuration, then this produces $2 \cdot \frac{1}{2} n\,(n+1)$ configurations that are in $\mathcal{T}_k$. This procedure generates all the elements of $\mathcal{T}_k$, but again overcounts the graphs that can be formed by different gluings, which were exactly the ones that did not have a unique definition of bubble time and that were overcounted in the iterative model. Perhaps a method can be found to generate all these graphs uniquely, or a characterization of the top and bottom partitions of line elements. However, we can give an upper limit of the number of topological graphs in $\mathcal{T}_k$ with this

restriction:

$$\begin{aligned} |\mathcal{T}_k| &\leq \sum_{T\in\mathcal{T}_{k-1}} 2\cdot\frac{1}{2}|x_k|\left(|x_k|+1\right) \\ &\leq \sum_{T\in\mathcal{T}_{k-1}} 2(k-1)\left(2(k-1)+1\right) \qquad (64) \\ &\leq (2k-1)! \qquad (65) \end{aligned}$$

In order to generalize this to the unrestricted case, one should add the option of connecting the vertices on top of the configuration in $\mathcal{T}_{k-1}$ to each other.

3.5 Iterative bubble addition and overcounting

In this section we revisit the iterative bubble addition model and calculate the one-bubble and two-bubble propagators.

3.5.1 Another approach

It could be the case that the iterative model has the same limiting behaviour as bubble gCDT itself. We note that 5 out of the 6 elements of $\mathcal{T}_2$ have a unique gluing order. For $\mathcal{T}_3$ holds that 42 of 57 elements have a unique gluing order and thus a uniquely defined bubble time.
The first step in trying to solve the iterative model is to calculate the one-bubble propagator B_1, which plays a fundamental role in the iterative bubble complex propagator B_{it} which satisfies a Dyson equation:

$$\mathbf{B}_{it}(a,b) = \delta_{a,b} + \sum_k B_1(a,k)\mathbf{B}_{it}(k,b). \qquad (66)$$

The one-bubble propagator itself is not affected by overcounting, and therefore this is also the correct one-bubble propagator of bubble gCDT.

3.5.2 The one-bubble propagator

We have already computed the combinatorial factor that corresponds to decorating the spatial skeleton of a bubble with edges in Claim 3.5. To compute all possible ways to add a bubble such that the initial ring has a vertices and the final ring has b vertices, we can sum the number of covered vertices N from 1 to $a-1$ and let the number of covered vertices M compensate to meet the boundary conditions:

$$M = b - a + N. \qquad (67)$$

Taking into account the a possible starting positions of the bubble, we obtain the following expression.

$$\begin{aligned} B_1(a,b) &= a\sum_{N=1}^{a-1} g^{2N+b-a}\tilde{g}^2\binom{2N+b-a}{N-1} \qquad (68)\\ &= \frac{a\tilde{g}^2 g^{2+b-a}\left(1+\sqrt{1-4g^2}\right)^{a-b}}{2^{a-b}\sqrt{1-4g^2}} \\ &\quad - a\tilde{g}^2 g^{a+b}\binom{a+b-2}{a-1} \\ &\quad {}_3F_2\left(\left[1,\frac{a+b}{2},\frac{a+b-1}{2}\right],[a,b],4g^2\right). \qquad (69)\end{aligned}$$

Here ${}_3F_2$ is a generalized hypergeometric function. Its definition is as follows:

$${}_{|n|}F_{|d|}\left([n_1,n_2,\ldots],[d_1,d_2,\ldots],z\right) = \sum_{k=0}^{\infty}\frac{z^k\prod_{i=1}^{|n|}(n_i)_k}{k!\prod_{j=1}^{|d|}(d_i)_k}, \qquad (70)$$

with $|n|$ and $|d|$ the lengths of the first and second slots of arguments and with

$$(a)_k = \frac{\Gamma(a+k)}{\Gamma(k)} = a(a+1)\ldots(a+k-1) \qquad (71)$$

the Pochhammer function. This sum was performed using the non-trivial Wilf-Zeilberger algorithm in Maple [38].
Both terms in B_1 seem to have special behaviour as $g \to 1/2$ or $4g^2 \to 1$. In plots it seems that the function shows more convergent behaviour towards this limit, but this has not yet been studied in detail.

3.5.3 Counting the overcounting

If one could keep track of the overcounting generated by the iterative bubble addition, then perhaps we can divide out this factor and end up with the bubble gCDT bubble complex propagator after all. If we add all configurations generated by gluing two bubbles, but multiply configurations such as in 3.5a by a factor $1/2$, then we will end up with a sum over all inequivalent configurations. We split up the two-bubble propagator in a non-overlapping bubbles and an overlapping bubbles term.

$$B_2(a,b) = B_2(a,b)_{n.o.} + B_2(a,b)_{o.}. \qquad (72)$$

Let us first calculate the case without overlap. We get a general factor of a for choosing the beginning vertex of the first bubble. The first bubble should cover at most $a-3$ vertices, otherwise the second bubble does not fit next to the first. The second bubble can then be chosen to start in $\mathcal{A}(N_1,N_2) = a - N_1 - N_2 - 1$ positions, where N_1 and N_2 are the vertices covered by bubble 1 and 2 respectively, as illustrated in Figure 3.11. The number of vertices on top of the respective bubbles we call M_1 and M_2 and we define $N = N_1 + N_2$ and $M = M_1 + M_2$.

$$B_2(a,b)_{n.o.} = \frac{a}{2}\sum_{N=1}^{a-2}\sum_{\{N_1,N_2\}}\sum_{\{M_1,M_2\}}\mathcal{M}(N_1,M_1)\mathcal{M}(N_2,M_2)\mathcal{A}(N_1,N_2)g^{M+N-4}\tilde{g}^4. \qquad (73)$$

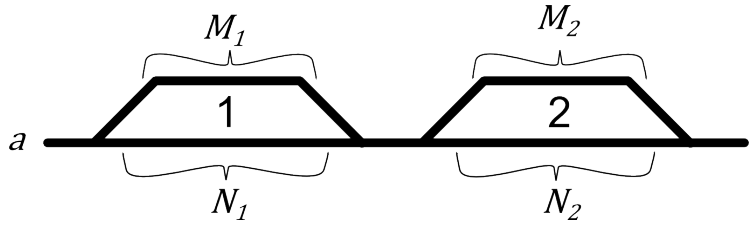

Figure 3.11: The number of covered vertices underneath bubble 1 and 2 we call N_1 and N_2 respectively. The new vertices on top of the bubbles we call M_1 and M_2.

Here $\{N_1, N_2\}$ are such that $N_1, N_2 \geq 1$ and $N_1 + N_2 = N$ and $\{M_1, M_2\}$ are such that $M_1, M_2 \geq 1$ and $M_1 + M_2 = M = b - a + N$. We could also sum over only N_1 and M_1 and replace N_2 and M_2 with $N - N_1$ and $M - M_1$ respectively. Working this out we obtain:

$$\begin{aligned} B_2(a,b)_{n.o.} &= \frac{a}{2}\tilde{g}^4 \sum_{N=1}^{a-1} (a-N-1) g^{b-a+2N-4} \\ &\quad \sum_{N_1=1}^{N-1} \sum_{M_1=1}^{b-a+N-1} \binom{N_1+M_1-2}{M_1-1} \binom{b-a+2N-M_1-N_1-2}{N-N_1-1}. \end{aligned} \tag{74}$$

For the overlapping case we use the labelling of the lengths of the line elements as indicated in Figure 3.12.

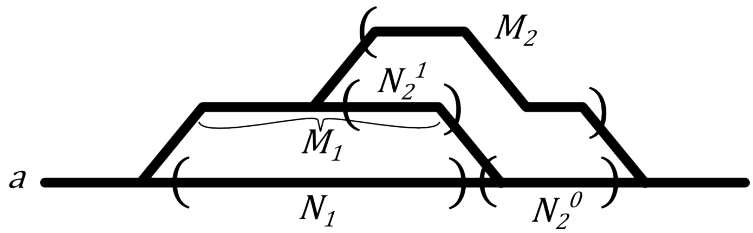

Figure 3.12: The labelling of the lengths for two overlapping bubbles. As before, N_1 and M_1 are respectively covered and created by the first bubble. The second bubble covers $N_2 = N_2^0 + N_2^1$ vertices of which N_2^0 are part of the original ring and N_2^1 are on top of the first bubble. On top of the second bubble there are M_2 vertices.

The line element that is labelled by N_2^1 is in between the two bubbles and therefore is "free", meaning that we have an unbounded sum over its length. We introduce again a parameter $\mathcal{A}$ that counts the number of possible locations for the second bubble.

$$\begin{aligned} B_2(a,b)_{o.} &= a \sum_{N_2^1=0}^{\infty} \sum_{\{N_1, N_2^0, M_1, M_2\}} g^{(M_1+N_1-2)+(M_2+N_2-2)} \tilde{g}^4 \\ &\quad \mathcal{A}(a, N_1, M_1, N_2^0, N_2^1) \mathcal{M}(N_1, M_1) \mathcal{M}(N_2, M_2), \end{aligned} \tag{75}$$

where the set $\{N_1, N_2^0, M_1, M_2\}$ is bounded by several equations. They satisfy the boundary conditions:

$$b = a - N_1 - N_2^0 + (M_1 - N_2^1) + M_2. \tag{76}$$

The first bubble fits on the ground and the second bubble fits on top of it:

$$1 \leq \quad N_1 \quad \leq a-1 \tag{77}$$
$$M_1 \quad \geq \max\{N_2^1, 1\}. \tag{78}$$

The floor level of the second bubble fits on the ground and can be empty, but the second bubble covers at least one vertex:

$$0 \leq \quad N_2^0 \quad \leq a - N_1 \tag{79}$$
$$N_2^0 + N_2^1 = \quad N_2 \quad \geq 1. \tag{80}$$

Lastly there is at least one vertex on top of the second bubble:

$$M_2 \geq 1. \tag{81}$$

For the number of positions of the second bubble $\mathcal{A}$ we have six different cases, illustrated in Figure 3.13.

$$N_2^0 = 0;\ N_2^1 > 0 \qquad \mathcal{A} = M_1 - N_2^1 + 1 \tag{82}$$
$$0 < N_2^0 < a - N_1;\ N_2^1 = 0 \qquad \mathcal{A} = 2 \tag{83}$$
$$N_2^0 = a - N_1;\ N_2^1 = 0 \qquad \mathcal{A} = 1 \tag{84}$$
$$0 < N_2^0 < a - N_1;\ 0 < N_2^1 < M_1 \qquad \mathcal{A} = 2 \tag{85}$$
$$0 < N_2^0 < a - N_1;\ N_2^1 = M_1 \qquad \mathcal{A} = N_2^0 + 1 \tag{86}$$
$$N_2^0 = a - N_1;\ 0 < N_2^1 < M_1 \qquad \mathcal{A} = N_2^1 + 1 \tag{87}$$

For more than two bubbles the problem becomes far more complicated, as we will need to start taking into account the distances between the first two bubbles to decide where our third bubble can be placed. There will also be far more cases for counting the number of possible locations of the three bubbles.

3.5.4 Future projects

Both the one-bubble propagator and the two-bubble propagator presented here can be used to study a simplified model of bubble gCDT with only a limited number of bubbles per spatial layer. It should be noted that these sums are not particularly easy to study. The fact that the one-bubble propagator seems to have special behaviour at the same value of g as CDT itself is a promising result.
In such a model the number of *sst*-triangles is always bounded by a constant times the number of strips, therefore one cannot properly study the influence of the second coupling constant $\tilde{g}$ that was not yet present in CDT. However, if the combinatorics of such a reduced model already yield a superexponential increase in the number of configurations for a given number of building blocks (see section 1.2.2), then this behaviour will also present itself in the general bubble gCDT model, which possesses more different configurations.

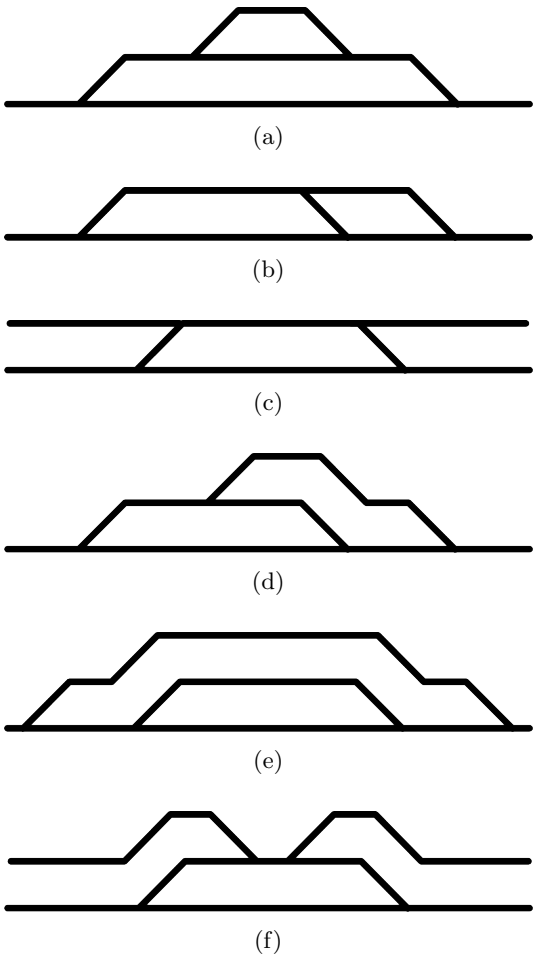

Figure 3.13: Pictures corresponding to the different bubble configurations. Figures (a), (b), (c), (d), (e) and (f) correspond to the cases (82), (83), (84), (85), (86) and (87) respectively.

4 Matrix Models

Matrix models are a method to generate an ensemble of weighted graphs as the Feynman graphs of a matrix field theory. The graphs are generated using local conditions on the valence of the vertices and the number of sides in a loop. One can also add colours to the edges and restrict the way these colours connect to each other. It is therefore possible to describe CDT and spiral gCDT in terms of a matrix model. Unfortunately both these models turn out to be hard to solve.

4.1 Introduction to Matrix Models

We start with an introduction to the basics of matrix models. See also [21] for a quick introduction and [26, 22, 20] for a more thorough description.

4.1.1 Calculating expectation values

As in the path integral approach, we define an unnormalized probability functional $\mathcal{Z}_0$:

$$\mathcal{Z}_0(N) = \int dM\, e^{-N \operatorname{Tr}\left(\frac{M^2}{2}\right)}. \tag{88}$$

The integration range and measure are well-defined, namely, to be the $N \times N$ Hermitian matrices $H(N)$ and the Haar measure on them,

$$dM = \prod_i dM_{ii} \prod_{i<j} d\operatorname{Re}(M_{ij}) d\operatorname{Im}(M_{ij}). \tag{89}$$

For a function $f : H(N) \to T(\mathbb{R}^N)$, where $T(\mathbb{R}^N) = \oplus_{k\geq 0} \left(\mathbb{R}^N\right)^{\otimes k}$ is the tensor algebra of $\mathbb{R}^N$, we define the expectation value of f as:

$$\langle f \rangle = \frac{1}{\mathcal{Z}_0(N)} \int dM\, e^{-N \operatorname{Tr}\left(\frac{M^2}{2}\right)} f(M). \tag{90}$$

We can calculate this expectation value for any f by expanding f in terms of products and sums of matrix coefficients. We use a trick called a *source integral* to calculate the expectation value of the products of matrix coefficients themselves.

$$\begin{aligned} \Sigma(S) &= \left\langle e^{\operatorname{Tr}(SM)} \right\rangle \\ &= \frac{1}{\mathcal{Z}_0(N)} \int dM\, e^{-N \operatorname{Tr}\left(\frac{M^2}{2} + SM\right)} \\ &= e^{\operatorname{Tr}\left(\frac{S^2}{2N}\right)}. \end{aligned} \tag{91}$$

In the last step we completed the square in the exponential, see also subsection 4.1.7. Through derivation we can now obtain the expectation value of any product of matrix coefficients. For example:

$$\begin{aligned}
\langle M_{ij}M_{kl}\rangle &= \left\langle \frac{\partial}{\partial S_{ji}}\frac{\partial}{\partial S_{lk}} e^{\mathrm{Tr}(SM)} \right\rangle \Big|_{S=0} \\
&= \frac{\partial}{\partial S_{ji}}\frac{\partial}{\partial S_{lk}} \Sigma(S)\Big|_{S=0} \\
&= \frac{\partial}{\partial S_{ji}}\frac{S_{kl}}{N} e^{\mathrm{Tr}\left(\frac{S^2}{2N}\right)}\Big|_{S=0} \\
&= \left(\frac{1}{N}\delta_{jk}\delta_{il} e^{\mathrm{Tr}\left(\frac{S^2}{2N}\right)} + \frac{S_{ij}S_{kl}}{N} e^{\mathrm{Tr}\left(\frac{S^2}{2N}\right)}\right)\Big|_{S=0} \\
&= \frac{1}{N}\delta_{jk}\delta_{il}. \qquad (92)
\end{aligned}$$

This expectation value of a quadratic term in M we will call the *propagator* and it will be fundamental in the description of other expectation values.
Note that we are tacitly interchanging derivations and integrals. This is allowed because the integrals are convergent. In general we have:

$$\langle M_{ij}M_{kl}\ldots\rangle = \frac{\partial}{\partial S_{ji}}\frac{\partial}{\partial S_{lk}}\ldots\Sigma(S)\Big|_{S=0}. \qquad (93)$$

When performing these derivations on $e^{\mathrm{Tr}\left(\frac{S^2}{2N}\right)}$ and setting $S = 0$, we notice two things. Firstly, an odd number of derivations is at least linear in S and vanishes, so the expectation value of an odd product of M's equals zero. Secondly, every term in the result corresponds to a complete pairing of the derivatives, or equivalently of the sets of indices. For every pair, one derivative acts on the exponential to take down a factor S/N and the other acts on this factor. This gives two delta functions relating the indices of the two derivations to each other, just as in the propagator (92). We can therefore relate every expectation value to sums of products of the quadratic expectation value (92). This is called *Wick's theorem* and the terms in the sum we call Wick contractions. For the expectation value of the tensor product of K matrices M we have:

$$\left\langle \prod_{k=1}^{K} M_{i_k j_k} \right\rangle = \sum_{p\in\mathcal{P}_K} \prod_{\{m,n\}\in p} \langle M_{i_m j_m} M_{i_n j_n}\rangle\,. \qquad (94)$$

Here $\mathcal{P}_K$ is the set of all partitions p of $\{1,\ldots,K\}$ into subsets of order two. These subsets of order two are unordered because, as we can see from the form of (92), $\langle MM\rangle$ is invariant under exchanging the position of the two matrices.
Since the expectation value is linear, we can take any contraction of the tensor on either side of (94) and bring the sums outside, such that the formula still holds. We will from now on restrict ourselves to working with scalar quantities, in particular scalar quantities that can be written as products of traces of products of M. This is equivalent to imposing the condition that all indices appear once in the first position and once in the second position. Because M is Hermitian, this guarantees exactly that the scalar is real.

4.1.2 Ribbon graphs

We will set up a correspondence between Wick contractions of a scalar quantity and a certain type of diagrams called ribbon graphs or fatgraphs. A ribbon graph is a graph where at every vertex, the adjacent edges are endowed with a cyclic order. This can be represented

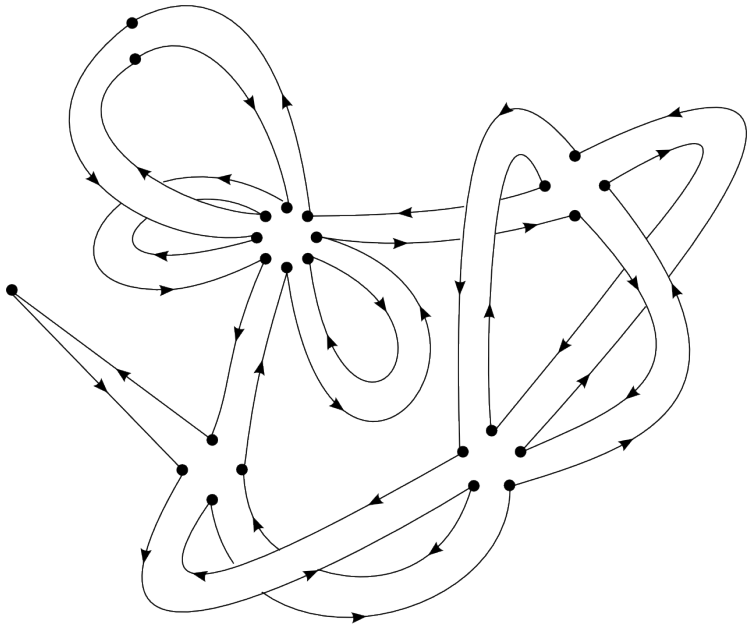

Figure 4.1: An example of a ribbon graph.

by drawing the vertices as a "circle" of dots, one for every connecting edge, and drawing the edges as two lines, or a "ribbon", of which both sides connect to adjacent dots of the vertex. See Figure 4.1 for an example. If we would allow the ribbons to be twisted around their own axis, then this would add extra freedom to the graph, therefore this is disallowed. To keep track of this, either side of the ribbon is endowed with an arrow in the opposite direction representing their orientation. The sides of the ribbons must then connect such that the orientation is preserved.
Ribbon graphs can be mapped to normal graphs by dropping the extra information. There is a one-to-one correspondence between ribbon graphs of a certain genus and graphs that can be embedded in a surface of that genus together with a specified embedding. The skeleton of any polygonization of a two-dimensional surface inherits such an embedding from the polygonization and can therefore be mapped to a unique ribbon graph.

4.1.3 Correspondence between Wick contractions and ribbon graphs

The way we relate ribbon graphs to expectation values of matrices is illustrated in Figure 4.2. The expression within an expectation value is initially related to a to a *starting diagram* in the following way. An index corresponds to one dot in a vertex. Every dot is connected to two half-edges with an incoming and an outgoing arrow, corresponding to the two appearances of the index in the first and second position. A matrix in a trace corresponds to half a ribbon between two dots, which represent its indices. A vertex or a circle of dots therefore represents a trace in the expectation value, on the left-hand side of (94). The starting diagram of $\langle \mathrm{Tr}(M^2)^2 \,\mathrm{Tr}(M^3)\,\mathrm{Tr}(M^4)\rangle$ would for example consist of two vertices with two dots and two half-ribbons, one vertex with three dots and three half-ribbons and one with four of either, as shown in Figure 4.3.
The Wick contractions correspond to all ways of pairing up the matrices and therefore they correspond exactly to the allowed ways of connecting the half-ribbons in the starting

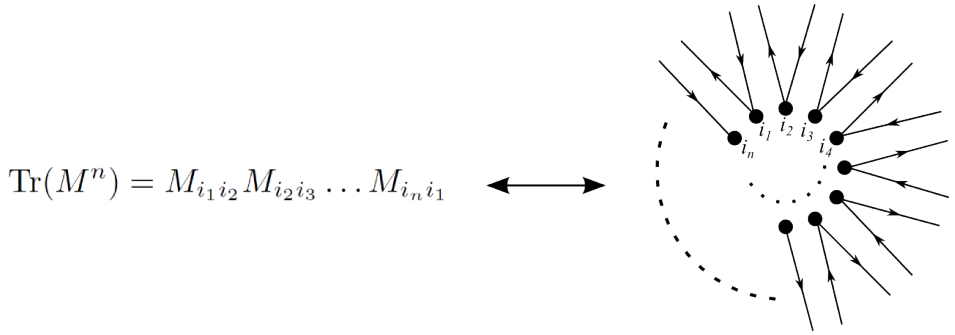

Figure 4.2: The correspondence between a trace of n matrices and the associated starting diagram.

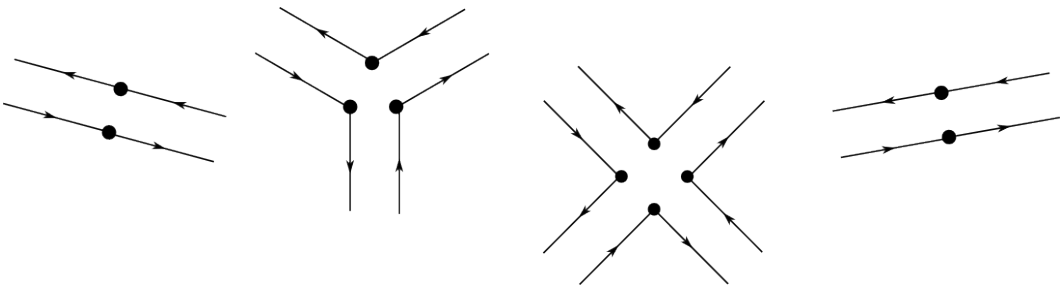

Figure 4.3: The starting diagram for $\left\langle \mathrm{Tr}(M^2)^2 \, \mathrm{Tr}(M^3) \, \mathrm{Tr}(M^4) \right\rangle$.

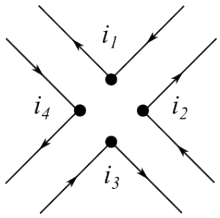

Figure 4.4: The starting diagram for the term $\mathrm{Tr}(M^4) = M_{i_1 i_2} M_{i_2 i_3} M_{i_3 i_4} M_{i_4 i_1}$.

diagram together to form a ribbon graph. Every ribbon itself then represents one of the propagators of the form $\langle MM \rangle$ on the right-hand side of (94). We can now relate Figure 4.1 to a contraction of $\big\langle \mathrm{Tr}(M)\,\mathrm{Tr}(M^2)\,\mathrm{Tr}(M^4)^2\,\mathrm{Tr}(M^5)\,\mathrm{Tr}(M^8) \big\rangle$.

4.1.4 Planar and non-planar diagrams

Let us perform the computation of the Wick contractions of $\big\langle \mathrm{Tr}(M^4) \big\rangle$ for illustration. We can represent the term we start with, $\mathrm{Tr}(M^4)$, as the diagram in Figure 4.4.
For the expectation value of this trace we have the following computation:

$$
\begin{aligned}
\big\langle \mathrm{Tr}(M^4) \big\rangle &= \sum_{\substack{i_1,i_2,\\ i_3,i_4}} \langle M_{i_1 i_2} M_{i_2 i_3} M_{i_3 i_4} M_{i_4 i_1} \rangle \\
&= \sum_{\substack{i_1,i_2,\\ i_3,i_4}} \sum_{p \in \mathcal{P}_4} \prod_{\{m,n\} \in p} \big\langle M_{i_m i_{m+1}} M_{i_n i_{n+1}} \big\rangle \\
&= \sum_{\substack{i_1,i_2,\\ i_3,i_4}} \Big(\langle M_{i_1 i_2} M_{i_2 i_3} \rangle \langle M_{i_3 i_4} M_{i_4 i_1} \rangle && (95) \\
&\qquad + \langle M_{i_1 i_2} M_{i_3 i_4} \rangle \langle M_{i_2 i_3} M_{i_4 i_1} \rangle && (96) \\
&\qquad + \langle M_{i_1 i_2} M_{i_4 i_1} \rangle \langle M_{i_3 i_4} M_{i_2 i_3} \rangle \Big) && (97) \\
&= \sum_{\substack{i_1,i_2,\\ i_3,i_4}} \frac{1}{N^2} \Big(\delta_{i_1 i_3} \delta_{i_3 i_1} + \delta_{i_1 i_4} \delta_{i_2 i_3} \delta_{i_2 i_1} \delta_{i_3 i_4} + \delta_{i_2 i_4} \delta_{i_4 i_2} \Big) \\
&= \frac{N^3}{N^2} + \frac{N}{N^2} + \frac{N^3}{N^2}. && (98)
\end{aligned}
$$

The terms in the Wick contraction (95), (96) and (97) are represented by the diagrams 4.5a, 4.5b and 4.5c respectively. The Wick contractions correspond precisely to all allowed ways to connect the ribbons of the labelled starting diagram 4.4. We see that if in every propagator the two matrices are multiplied, so share a common index, then the corresponding diagram is planar. If this is not the case, as for term (96), then the diagram becomes non-planar, as in Figure 4.5b, which can be viewed as a tesselation of the torus. The non-planar terms give rise to more delta functions which cancel the summations over the values of the indices. Therefore the planar diagrams contribute with a factor N, while the non-planar diagram contributes with, in this case, a factor $1/N$.

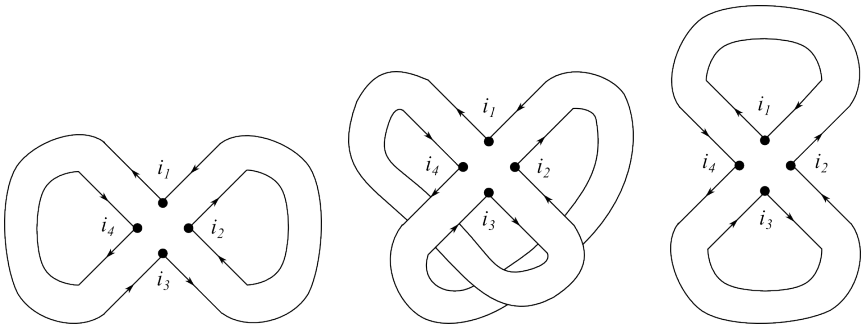

(a) Diagram corresponding to (95).

(b) Diagram corresponding to (96).

(c) Diagram corresponding to (97).

Figure 4.5: Ribbon graphs corresponding to the different Wick contractions of $\langle M_{i_1 i_2} M_{i_2 i_3} M_{i_3 i_4} M_{i_4 i_1} \rangle$. Note that (a) and (c) are the same under cyclic relabelling of indices.

This relates to a result that holds in general for matrix models. If we view a ribbon graph as a tesselation of a compact two-dimensional surface, then its contribution is proportional to $N^{e_2 - e_1}$, where e_i is the number of i-cells. See [21] for a detailed calculation of this result. For the genus g of a two-dimensional surface Σ we have:

$$2 - 2g = \chi(\Sigma) = e_0 - e_1 + e_2, \tag{99}$$

so for the order of a diagrams holds:

$$e_2 - e_1 = 2 - 2g - e_0. \tag{100}$$

We see that the order only decreases with genus, so the planar diagrams are the leading order in N. Therefore taking the $N \to \infty$ limit singles out the planar diagrams and this is what is usually done, because if all geni are taken into account, the number of configurations will in general grow superexponentially.

4.1.5 Generating specific ensembles

To illustrate how one might describe specific ensembles using matrix models, let us consider the expectation value of the generating function $f_3 = e^{N c_3 \operatorname{Tr}\left(\frac{M^3}{3}\right)}$.

$$\begin{aligned} \langle f_3 \rangle &= \sum_{k=0}^{\infty} \frac{(N c_3)^k}{3^k k!} \left\langle Tr\left(M^3\right)^k \right\rangle \\ &= \sum_{k=0}^{\infty} \frac{(N c_3)^k}{3^k k!} \sum_{T \in \tilde{\mathcal{X}}_k} \frac{N^{e_2(T)}}{N^{e_1(T)}}. \end{aligned} \tag{101}$$

Here $\tilde{\mathcal{X}}_k$ is the set of all ribbon graphs with k three-valent vertices, where all the dots are labelled with an index, as we have seen before in Figures 4.4 and 4.5. We would like to get rid of this labelling and sum over inequivalent diagrams. The order of the relabelling symmetry group of a ribbon graph with k three-valent vertices is $3^k k!/C_T$, where C_T again is the order of the symmetry group of the unlabelled diagram. Because the traces have a

cyclic symmetry, we are allowed to relabel cyclically the dots around every vertex, and this gives us the factor 3^k. The permutation of the different identical vertices gives us $k!$. Then we have to divide out the symmetry of the entire diagram because we will obtain the same labelled configuration multiple times if the diagram has some overall symmetry. We can now rewrite our expectation value in the following way:

$$\begin{aligned}\langle f_3 \rangle &= \sum_{k=0}^{\infty} \sum_{T \in \mathcal{X}_k} \frac{1}{C_T} \left(N^{e_0(T)-e_1(T)+e_2(T)} \right) c_3^k \\ &= \sum_{T \in \mathcal{X}} \frac{1}{C_T} \left(N^{\chi(T)} \right) c_3^{e_0(T)}, \end{aligned} \tag{102}$$

where $\mathcal{X}_k$ is the set of unlabelled inequivalent graphs with k three-valent vertices and $\mathcal{X} = \bigcup_k \mathcal{X}_k$ is the collection of all inequivalent ribbon graphs with three-valent vertices. By taking an $N \to \infty$ limit we can single out the planar diagrams, that are a tesselation of one or multiple spheres, and at the same time get rid of the N dependence, which is irrelevant for our ensemble of diagrams.

$$\begin{aligned}\lim_{N\to\infty} \frac{\langle f_3 \rangle}{N^2} &= \lim_{N\to\infty} \sum_{T \in \mathcal{T}} \frac{1}{C_T} N^{-g} c_3^{e_0} \\ &= \sum_{T \in \mathcal{T}} \frac{1}{C_T} c_3^{e_0} \end{aligned} \tag{103}$$

Now the sum starts to resemble some of the sums that we have seen before. In particular, there is a one-to-one mapping between the ribbon graphs with three-valent vertices and triangulations of the same topology, see subsection 4.2.1. Therefore we might as well view (103) as a sum over triangulations that are tesselations of one or multiple spheres, where we give every triangle a weight c_3.
We can furthermore add two special vertices to the triangulation that we associate to two boundaries. If we now also subtract the diagrams that are disconnected, then the diagrams we end up with will have the topology of a cylinder, and the ensemble we sum over is proportional to the grand canonical path sum of Dynamical Triangulations in two dimensions. In formula this looks as follows. First we define a new "expectation value" for a function g:

$$\langle g \rangle_3 = \langle f_3 g \rangle \,. \tag{104}$$

The path sum of DT can then be described as follows:

$$Z_{DT} \propto \sum_{a,b} \lim_{N\to\infty} \frac{1}{N^2} \left\langle \mathrm{Tr}(M^a)\, \mathrm{Tr}(M^b) \right\rangle_3 - \langle \mathrm{Tr}(M^a) \rangle_3 \left\langle \mathrm{Tr}(M^b) \right\rangle_3 . \tag{105}$$

We call $S = N \,\mathrm{Tr}\left(\frac{M^2}{2} - c_3 \frac{M^3}{3} \right)$, which is minus the term in the exponential of the probability functional for $\langle . \rangle_3$, the action of this matrix model. By adapting S we can study many different ensembles of weighted graphs.

4.1.6 Multi-matrix models

One can introduce colours in a matrix model by introducing different integration variables, say A and B, both ranging over Hermitian matrices. The edges correspond to propagators and therefore to the quadratic terms in the action. If we add terms of the form A^2 and B^2

to the action, but not of the form AB, then only propagators of the form $\langle AA\rangle$ or $\langle BB\rangle$ are non-zero and the edges will be endowed with either colour A or colour B. Adding a term of the form AAB to the action will then generate three-valent vertices in the resulting diagrams that connect two A and one B edge. A model with multiple integration variables we call a multi-matrix model.

4.1.7 Dually weighted matrix models

Apart from restricting only the valence of the vertices in the diagrams generated by a matrix model, one can also simultaneously restrict the number of edges of the polygons. Models of this type are called dually weighted. The trick is to give the quadratic terms in the action a weight in the form of an external $N \times N$ matrix C that is invertible and Hermitian.

$$\mathcal{Z}_C(N) = \int dM\, e^{-N \operatorname{Tr}\left(\frac{\left(C^{-1}M\right)^2}{2}\right)} \tag{106}$$

The source integral Σ will now depend on C. We define

$$\Sigma = \frac{1}{\mathcal{Z}_C} \int dM\, e^{-\frac{N}{2}\operatorname{Tr}\left((C^{-1}M)^2\right)+\operatorname{Tr}(SM)}. \tag{107}$$

We substitute $M' = C^{-1}M$ and complete the square in the exponent.

$$\begin{aligned} -\frac{N}{2}\operatorname{Tr}\left[M'^2 - \frac{2}{N}SCM'\right] &= -\frac{N}{2}\operatorname{Tr}\left[M'^2 - \frac{SCM'}{N} - \frac{M'SC}{N}\right] && (108)\\ &= -\frac{N}{2}\operatorname{Tr}\left[\left(M' - \frac{SC}{N}\right)^2 - \left(\frac{SC}{N}\right)^2\right] && (109)\\ &= -\frac{N}{2}\operatorname{Tr}\left[(C^{-1}M'')^2\right] + \frac{\operatorname{Tr}\left[(SC)^2\right]}{2N}, && (110) \end{aligned}$$

where we have substituted $C^{-1}M'' = M' - \frac{SC}{N}$. So the source integral evaluates to:

$$\Sigma(S) = e^{\frac{\operatorname{Tr}\left((SC)^2\right)}{2N}}. \tag{111}$$

The propagators will then similarly depend on C.

$$\begin{aligned} \langle M_{ij}M_{kl}\rangle_C &= \frac{\partial}{\partial S_{ji}}\frac{\partial}{\partial S_{lk}} e^{\frac{\operatorname{Tr}\left((SC)^2\right)}{2N}}\Big|_{S=0}\\ &= \frac{\partial}{\partial S_{ji}}\left(\frac{1}{N}C_{ka}S_{ab}C_{bl}\right) e^{\frac{\operatorname{Tr}\left((SC)^2\right)}{2N}}\Big|_{S=0}\\ &= \frac{1}{N}C_{kj}C_{il} \end{aligned} \tag{112}$$

In a ribbon graph a single complete ribbon represents a propagator and, as Figure 4.6 illustrates, every side of such a ribbon corresponds precisely to a factor $C/\sqrt{N}$. A polygon with k sides, which is a closed loop in the diagram, therefore corresponds to a trace over k matrices C divided by $N^{k/2}$. One can now subject the diagrams to conditions on the number of sides by maintaining the conditions on C of the form

$$\operatorname{Tr}\left(C^k\right) = N\, t_k, \tag{113}$$

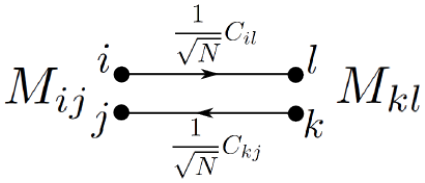

Figure 4.6: The corresponding diagram of the propagator $\langle M_{ij}M_{kl}\rangle_C = \frac{1}{N}C_{kj}C_{il}$. We see that in the diagram, the indices come out in such a way that both sides of the ribbon correspond precisely to a factor $C/\sqrt{N}$.

where t_k is the weight of a k-sided polygon. The factor N stems from the fact that we are taking a trace. Compare to the case without an external C factor, where a k-loop corresponds to a trace of $\delta^k/N^{k/2} = N/N^{k/2} = (N\cdot 1)/N^{k/2}$ and the faces have weight 1 in for example (102).

Let us consider a general generating function $f = e^{N\sum_i c_i \operatorname{Tr}\left(\frac{M^i}{i}\right)}$. If the matrix C satisfies (113) for some real weights t_k, $k\in\mathbb{N}$, then in generalization of (102) the expectation value of f evaluates to:

$$\langle f\rangle_C = \sum_{\Gamma\in\mathcal{G}} \frac{1}{C_\Gamma} N^{\chi(\Gamma)} \prod_i c_i^{e_0[i](\Gamma)} t_i^{e_2[i](\Gamma)}, \tag{114}$$

where $e_j[i](\Gamma)$ stands for the number of j cells of valence i of the ribbon graph Γ, and $\mathcal{G}$ is the collection of all ribbon graphs. By setting various weights c_i and t_i to zero, we can adapt both the allowed vertex valences and the number of sides of the polygons of the graphs.
One should note that for any finite N, it is of course not possible to require an infinite number of independent conditions of the form (113). In many cases, the conditions can only be required in the $N\to\infty$ limit. This poses a problem for solving such a model, which would require some knowledge of the behaviour of a family of matrices $C(N)$ satisfying (113) in the limit. Kazakov et al. discovered a rule for the characters of such a family in [34]. See also [33] for a review of this method.

4.2 Matrix Model for CDT

We will present a slightly modified version of the matrix model for CDT introduced by Benedetti and Henson in [15]. It is a dually weighted bicoloured model, such that in the $N\to\infty$ limit, there is a one-to-one correspondence between the CDT triangulations and their weights, and the ribbon graphs that contribute to the transition between two spatial boundary loops, and their amplitudes. There is also at least one other matrix model description of CDT that relies on other principles, see [2].

4.2.1 Dual triangulations

Instead of a direct mapping between the ribbon graphs and the CDT triangulations, we first map our triangulations to their *Poincaré dual*. For a two-dimensional polygonization we can define the dual in the following way:

- A polygon is replaced by a vertex with as many connecting edges as the polygon has sides;
- A vertex is replaced by a polygon with as many sides as the valence of the vertex;

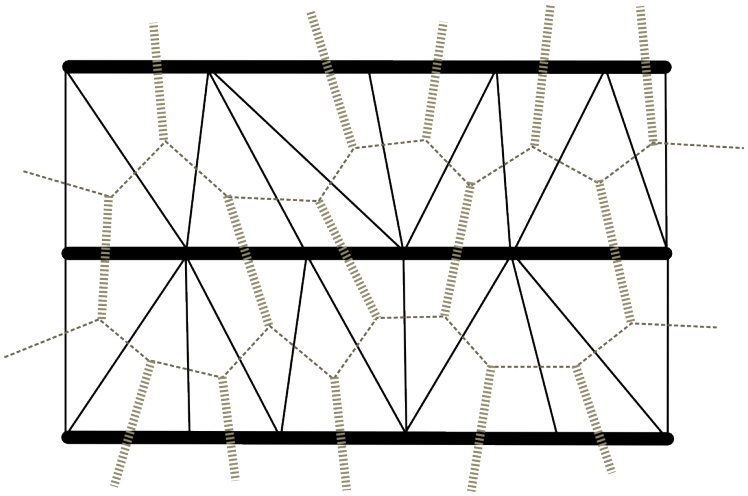

Figure 4.7: Illustration of the dual (dotted) of a 2D CDT triangulation.

- An edge is then automatically replaced by an edge that crosses the original one.

Figure 4.7 shows the dual of a two-dimensional CDT triangulation. Here the dual edges retain the colour of the original edges. We see that for the dual configurations holds that every vertex has colour tts and every polygon has precisely two s-sides. We see that we can give the following definition of a dual CDT triangulation.

Definition 4.1. A **dual CDT triangulation** is a bicoloured polygonization satisfying the following conditions:

(i) *(tts)*: Every vertex has two adjacent t-edges and one adjacent s-edge, except for the boundary vertices;

(ii) *(Colouring condition)*: Every polygon has precisely two s-sides;

(iii) *(Boundary condition)*: There are two "boundary vertices" with only s-edges, one is labelled initial and the other final.

4.2.2 A matrix model for CDT

We can now define a matrix model that generates dual CDT triangulations with the appropriate weights. It is essential for this description that CDT can be generated locally, as we have seen in section 2.1. We formulate conditions on the matrix model such that the generated graphs satisfy the conditions in definition 4.1. The two colours s and t correspond to two integration variables we call S and T. The tts-vertices are generated by a term $gTTS$ in the action, where g is the weight of a tts-triangle in CDT. The appearance of precisely two s-edges in every polygon is implemented by working with an external matrix C. We define the following probability functional:

$$\mathcal{Z}_{dCDT} = \int dT\, dS\, e^{-N \operatorname{Tr}\left(\frac{1}{2}T^2 + \frac{1}{2}(C^{-1}S)^2 - gTTS\right)} \tag{115}$$

with on the matrix C the condition

$$\operatorname{Tr}(C^m) = N\delta_{2,m} \qquad (\forall m) \text{ as } N \to \infty. \tag{116}$$

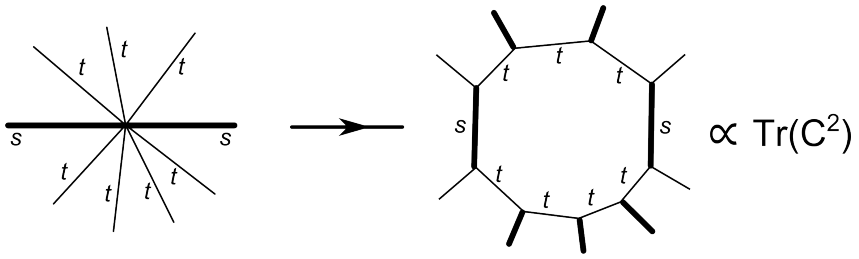

Figure 4.8: A polygon with two s-edges is proportional to the right-hand side of (116) for $m = 2$, which is the only case for which the expression is non-zero.

Formula (116) captures the condition that every polygon containing s-edges has precisely two of them, as illustrated in Figure 4.8. We are not constraining the loops with only t-edges, which correspond to vertices with only t-edges or "caps" in the normal CDT model. However, it is clear from Corollary 2.12 that only two of these can appear in a graph that is a tesselation of the sphere and satisfies the conditions in Definition 4.1.
Just as we have done for DT in the subsection 4.1.5, we can add boundaries to our ribbon graphs by adding an initial and final vertex. We then have the following correspondence between the diagrams and weights generated by this model and the triangulations and weights of CDT.

$$\begin{aligned} Z_{CDT} &\propto \sum_{a,b} G(a,b) \\ &= \sum_{a,b} \lim_{N\to\infty} \frac{1}{N^2} \left(\left\langle \mathrm{Tr}(S^a)\,\mathrm{Tr}(S^b) \right\rangle - \left\langle \mathrm{Tr}(S^a) \right\rangle \left\langle \mathrm{Tr}(S^b) \right\rangle \right) \end{aligned} \tag{117}$$

Here $G(a,b)$ is the propagator for CDT we have introduced in section 3.2, for $a, b \in \mathbb{N}$. A connected graph with two boundary vertices will not have any caps. The disconnected graphs are subtracted in the second term of (117).
Benedetti and Henson tried various routes to solving this model, but did not succeed.

4.3 Generalization for gCDT

The model presented in the previous section can be generalized to a matrix model for spiral gCDT.

4.3.1 Dual of spiral gCDT

As was the case with CDT, we can map spiral gCDT to its dual.

Definition 4.2. Dual spiral gCDT triangulation
A dual of a spiral gCDT triangulation is a bicoloured polygonization satisfying the following conditions:

(i) (*tts and sst*): Every vertex is coloured either *tts* or *sst*, except for the boundary vertices;

(ii) *(Lightcone colouring condition)*: If we go around a polygon, we encounter a group of edges of every colour twice;

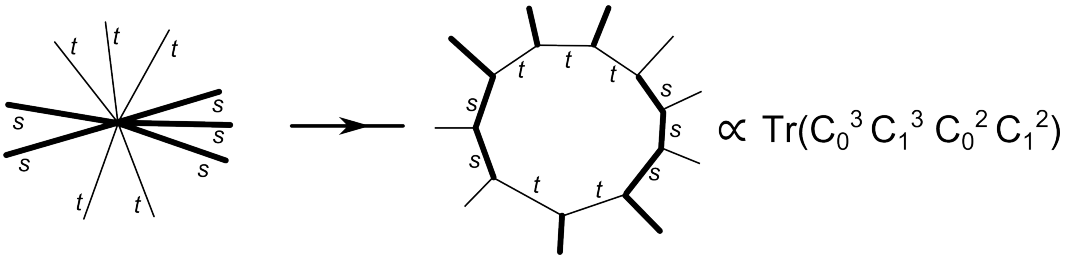

Figure 4.9: A polygon that satisfies the light cone colouring condition is proportional to a trace of a product of the form $C_0^{i_1} C_1^{j_1} C_0^{i_2} C_1^{j_2}$, for positive and non-zero integers i_1, j_1, i_2, j_2. This is precisely the type of trace that gets a non-zero weight if we impose condition (119).

(iii) *(Boundary condition)*: There are two "boundary vertices" with only s-edges, one is labelled initial and the other final.

4.3.2 A matrix model for spiral gCDT

We can generalize the model by Benedetti and Henson to the dual of spiral gCDT by symmetrizing the action. We include both a term $gTTS$ for the tts-vertex as well as a term $\tilde{g}SST$ for the sst-vertices, which get a weight $\tilde{g}$. Also do we now have to weight both S and T with an external matrix. We define the following probability functional:

$$\mathcal{Z}_{dgCDT} = \int dT\, dS\, e^{-N \operatorname{Tr}\left(\frac{1}{2}(C_0^{-1}T)^2 + \frac{1}{2}(C_1^{-1}S)^2 - gTTS - \tilde{g}SST\right)}, \tag{118}$$

where the external matrices satisfy in the $N \to \infty$ limit

$$\operatorname{Tr}\left(\prod_{\substack{k=1 \\ i_k, j_k \in \mathbb{N}_{\geq 1}}}^{m} C_0^{i_k} C_1^{j_k} \right) = N \delta_{2,m} \qquad (\forall m) \tag{119}$$

$$\operatorname{Tr}\left(C_0^m\right) = 0 \qquad (\forall m) \tag{120}$$

$$\operatorname{Tr}\left(C_1^m\right) = 0 \qquad (\forall m). \tag{121}$$

How condition (119) translates the colouring condition is illustrated in Figure 4.9. This time we are also prohibiting the appearance of caps, timelike or spacelike, by imposing conditions (120) and (121). As the timelike directed walks can now not end without the addition of boundaries and the configurations are finite, there will not be any "vacuum graphs" for this model. By this we mean that without the addition of boundaries or source terms, the set of graphs in its expansion will be empty.
We then have the following correspondence between spiral gCDT and the weighted graphs

generated by this model:

$$\begin{aligned} Z_{gCDT} &\propto \sum_{a,b} G(a,b) \\ &= \sum_{a,b} \lim_{N\to\infty} \frac{1}{N^2} \left(\left\langle \mathrm{Tr}(S^a)\,\mathrm{Tr}(S^b) \right\rangle - \left\langle \mathrm{Tr}(S^a) \right\rangle \left\langle \mathrm{Tr}(S^b) \right\rangle \right) \\ &= \sum_{a,b} \lim_{N\to\infty} \frac{1}{N^2} \left\langle \mathrm{Tr}(S^a)\,\mathrm{Tr}(S^b) \right\rangle . \end{aligned} \tag{122}$$

As we have seen in section 2.1 the locally generated CDT triangulations and therefore their dual triangulations are automatically connected, and therefore the disconnected term vanishes. There can be no graphs with only one boundary.

4.4 How to solve the matrix models

In general matrix models cannot be solved, but there are a few standard approaches to determining the limiting behaviour of the integrals that deal with for example diagonalization of the integration variables. A thorough explanation of a number of methods can be found in [20, 26, 22]. Many of these standard methods do not seem to apply to either of the models described above. Benedetti and Henson have used several techniques in their paper, but were in the end not able to solve the model.
One thing that can be done straightforwardly for the CDT model is integrating out the variable S, using again a completion of the square in the exponent of $\mathcal{Z}_{dCDT}$. This corresponds in the CDT diagrams to gluing all tts-triangles together in pairs along their s-edges. The T variable can also be integrated out and this corresponds to gluing the triangles into strips and considering the combinatorics of these strips, which is similar to the strip propagator approach that we studied in Chapter 3. In this case the resulting transformation determinant will play an important role. Methods for how to deal with these can be found in [40].
For the spiral gCDT model, the variables S and T can also be integrated out. The integration of the T variable corresponds to an approach similar to the strip propagator approach for bubble gCDT, where now beside strips and bubbles, we should also consider the spirals as separate objects and the bubbles are allowed to overlap each other. The resulting matrix model represents the combinatorics of gluing these three objects, strips, bubbles and spirals, to each other in all possible ways satisfying the boundary conditions. Integration of the T variable represents a very similar approach in the timelike direction, which we will also shortly discuss in subsection 5.1.2. For both approaches a transformation determinant will play a role.
For the application of character expansion methods to these models [35] will be of help. The formula by Kazakov et al. in [34] can be applied to the situation in the CDT case, to explore the behaviour of a family of matrices satisfying (116). For the condition (119) that mixes the two external matrices in the gCDT model however, no such formula exists.

4.5 Dual models

Models that can be presented in the form of a dually weighted matrix model, can always be presented as such in two ways, namely, we can also write down a dual matrix model. In the case of the matrix model for the dual of CDT, we can also construct a model for CDT itself as follows. We define the probability functional

$$\mathcal{Z}_{CDT} = \int dT\, dS\, e^{-N \operatorname{Tr}\left(\frac{1}{2}(C_0^{-1}T)^2 + \frac{1}{2}(C_1^{-1}S)^2 - \sum_{k,l} T^k S T^l S\right)} \tag{123}$$

with

$$\operatorname{Tr}\left(C_0^2 C_1\right) = N\, g \tag{124}$$

and then we have

$$G(a,b)_{CDT} \quad = \quad \lim_{N\to\infty} \left(\left\langle \operatorname{Tr}(S^a) \operatorname{Tr}(S^b) \right\rangle - \left\langle \operatorname{Tr}(S^a) \right\rangle \left\langle \operatorname{Tr}(S^b) \right\rangle \right) \tag{125}$$

Analogously we can define for spiral gCDT:

$$\mathcal{Z}_{gCDT} = \int dT\, dS\, e^{-N \operatorname{Tr}\left(\frac{1}{2}(C_0^{-1}T)^2 + \frac{1}{2}(C_1^{-1}S)^2 - \sum_{k,l,m,n} T^k S^l T^m S^n\right)}, \tag{126}$$

where in the sum k, l, m and n should be integers greater or equal to 1. On the external matrices we should then impose the conditions:

$$\operatorname{Tr}\left(C_0^2 C_1\right) \quad = \quad N\, g \tag{127}$$

$$\operatorname{Tr}\left(C_0^2 C_1\right) \quad = \quad N\, \tilde{g}. \tag{128}$$

We will then again have

$$G(a,b)_{gCDT} \quad = \quad \lim_{N\to\infty} \left(\left\langle \operatorname{Tr}(S^a) \operatorname{Tr}(S^b) \right\rangle - \left\langle \operatorname{Tr}(S^a) \right\rangle \left\langle \operatorname{Tr}(S^b) \right\rangle \right) \tag{129}$$

Both these models have far simpler conditions on the external matrices C_0 and C_1, but far more complex expressions in the exponentials, and therefore the odds of finding a solution are slim.

5 Other Methods

Here we discuss a few other ideas for studying the path sum of the two-dimensional gCDT models presented in this thesis.

5.1 Mappings of CDT and gCDT to other ensembles

In the study of random ensembles of geometric objects it can be useful to find a map from one ensemble of geometries to another. There are two kinds of these mappings that can be of use. The first is a one-to-one mapping, such as between CDT or spiral gCDT and their Poincaré dual, which we have used in Chapter 4 to construct a matrix model for either ensemble. The other is a one-to-many mapping, where the amount of degeneracy is under control. Examples of this are the maps from bubble gCDT to the spatial skeleton and to the topological graphs that we have defined in Chapter 3, where the degeneracy can be controlled by calculating the number of ways to decorate a skeleton with timelike edges and varying the line element lengths.

5.1.1 Relations between CDT and other ensembles

There are many maps from CDT to other geometrical ensembles. Most of them rely heavily on the linear order of the strips in CDT and cannot straightforwardly be generalized to gCDT. We give a few examples. In [23], Di Francesco et al. define one-to-one maps from the dual of CDT to trees and random walks. Durhuus et al. define in [25] another injective way to represent CDT triangulations as trees. They moreover define a many-to-one map to a reduced model in which all spatial layers are contracted to a point and use this to show that the spectral dimension of two-dimensional CDT equals two.

5.1.2 Digraphs

The strip propagator approach for gCDT makes use of a projection of bubble gCDT to the set of spatial skeletons. One can attempt an equivalent approach for the timelike skeleton of spiral gCDT. The advantage of this approach is that, as we have shown in section2.2.4, the timelike skeleton can be endowed with the structure of an acyclic digraph. Acyclic digraphs are also studied in the context of causal sets, see, for example, [18] and [27], although in that case there are no contraints on the planarity of the graphs. Also these digraphs do not come with an intrinsic embedding, while in our case the different embeddings of a graph should be considered as different configurations, or in other words, the amplitude of a digraph should be multiplied by the number of allowed embeddings. Indeed the great disadvantage of this approach is that the restrictions on these digraphs become rather complicated.
In the timelike skeleton there can appear the vertical equivalent of a strip, namely a set of stacked *sst*-triangles between the initial and final boundary. We will call such a structure a *gap*. If no gaps occur in the configuration, then the timelike digraph is connected and should be embeddable in a cylinder in such a way that the sources and sinks of the digraph occur on either boundary. If there is one gap, then the timelike skeleton is still connected, but the topology should be planar in such a way that there is an embedding in the plane for which the sources and sinks are separated and at the boundary of the embedding. If there is more than one gap, then more of these planar pieces occur, which should be endowed with an order.
The timelike digraph does completely determine the number of building blocks of either type, in the same way that the spatial skeleton of a bubble determines the number of triangles inside.

5.1.3 Digraphs for CDT

For CDT the projection to the timelike digraph is a one-to-one mapping, i.e. the timelike skeleton completely determines the triangulation. This map is also trivially related to the mapping of CDT to trees introduced by Durhuus et al. in [25], where the digraph is mapped to a tree by deleting the leftmost edge at every vertex.

5.2 Graph Theory

As the setup of our project can be interpreted as a problem in graph theory, we would like to use the advanced tools from this mathematical field of study. Unfortunately the ensemble we study is very specific and its difficulty lies precisely in the specific conditions, so many general results turn out not to be very helpful. One very strong theorem that could in principle be useful, if we can adapt the model to satisfy its prerequisites, is the Graph Minor Theorem [16]. It is a very strong result, whose proof was only finished in 2004. See for an elaborate introduction to the basics of graph theory for example [17].

5.3 Monte Carlo simulations

In CDT the Markov chain Monte Carlo method is used to study the typical states that arise from the CDT path sum in two and more dimensions for a given value or range of the number of building blocks N. It can be applied to study the $N \to \infty$ limit of these typical states, and with that the continuum behaviour of CDT. It can most likely be straightforwardly generalized to either of the two two-dimensional gCDT models described in this thesis.

5.3.1 How does it work?

The process works as follows. We have a set of options, in this case the set of different geometries $\mathcal{T}$, that are weighted by a probability functional, in this case the partition sum. We construct a set of steps or moves, which are small changes to the configurations such that we stay inside $\mathcal{T}$, but that are ergodic. By this we mean that any allowed configuration can be obtained from any other by applying a finite number of steps. For two-dimensional CDT the step of the creation or destruction of an s-edge by breaking up a vertex or gluing two together, as illustrated by Figure 5.1, is an ergodic move, that can generate all CDT triangulations from a minimal one [9]. The Monte Carlo moves for three- and four-dimensional CDT can be found in [11].
One now constructs a chain of configurations by picking one and applying the steps randomly, but with a certain weight that is based on the effect of the step on the weight of the configuration. This chain is Markovian in the sense that the order of the steps does not matter, i.e. the system does not have a memory of the previous steps other than how they in total have affected the configuration. By repeating this procedure we eventually end up in an equilibruim state of the system, where the qualitative behaviour of the configuration does not change anymore. By studying these equilibrium states for a large number of building blocks N, one can derive the limiting behaviour of the typical configuration and estimate the size of the (quantum) fluctuations around this average geometry.

5.3.2 Monte Carlo simulations for gCDT

By adapting the steps for two-dimensional CDT, it is most likely possible to construct a set of ergodic steps for either bubble gCDT or spiral gCDT. The three-dimensional analogues of these two models are already being studied using simulations, see [32]. One could imagine local steps that affect the vertices in such a way that precisely the light cone colouring

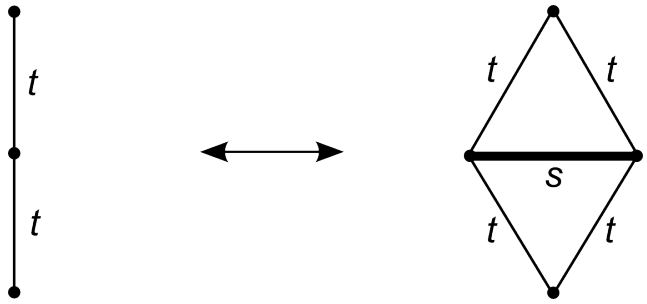

Figure 5.1: The step of creation and annihilation of an s-edge in a CDT triangulation.

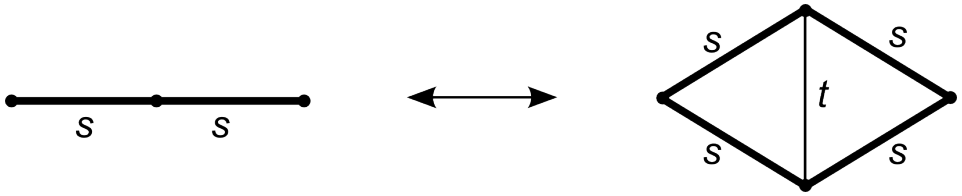

Figure 5.2: The step of creation and annihilation of a t-edge in a gCDT triangulation.

condition is preserved. This might render a way to study spiral gCDT using Monte Carlo simulations. Another approach would be to take the bubbles as fundamental objects and allow, next to the CDT steps, only steps that create or destroy a bubble of minimal size, as shown in Figure 5.2, and steps that enlarge or shrink the bubbles. Such a construction could perhaps be used to study bubble gCDT using Monte Carlo simulations.
Studying two-dimensional gCDT with the use of simulations will not provide us with an analytical solution of the path sum, but it will provide evidence on whether the universality class of either gCDT model is the same as that of two-dimensional CDT and it could provide additional input to work towards on the analytical front.

Discussion

This thesis discussed the two-dimensional version of a new generalization of CDT. Two related models were introduced, bubble gCDT and spiral gCDT, both relying on the introduction of a new triangle with two spacelike sides and one timelike side that was not present in the original two-dimensional CDT. The vertices in the triangulations associated to these models were submitted to a light cone colouring condition, which required that at every vertex we have the timelike edges pointing up and down and spatial edges to either side. We gave the proof of a few interesting properties of these configurations, in particular, the presence of an overall time direction.
If the gCDT approach would yield results that resemble the results of CDT itself, then this would tell us a lot about the role the time-layering plays in CDT. This thesis was therefore devoted to finding an analytical solution to either of the two proposed models. We discussed the strip propagator method for CDT and a similar approach for bubble gCDT. Solving the problem along this route would require an accessible classification of all possible spatial skeletons of bubble configurations and being able to compute a number of difficult sums. We constructed a simplified model where at every vertex we had maximally one bubble originating or ending, but although this seemed to simplify the calculation, the same difficulty of finding a characterization of topological graphs was met. We nonetheless computed the one-bubble propagator and started the computation of the two-bubble propagator, both of which can be used to study a reduced model that incorporates maximally one or two bubbles per layer.
We then dived into the realm of matrix models, where we presented the matrix model for CDT by Benedetti and Henson [15] and proposed a generalization along the same lines for gCDT. We discussed possible methods for solving these models and introduced the two dual models. In the last chapter we discussed a few other ideas that could eventually lead to other methods for solving either of the models.
As a next step one could indeed attempt to find a classification of the topological graphs that are needed to study bubble gCDT in the way we proposed in Chapter 3. In particular, to study the exact model one would need to categorize the combinatorial information captured in the order of the bubbles in such a graph. This would also be an interesting object of study from a mathematical point of view. Another approach would be to try to extract the leading order behaviour directly, instead of considering the model exactly.
The model of iterative bubble addition could have the same continuum behaviour as the gCDT models. The iterative propagator can at least be formulated and, in principle, calculated and this alone makes this model interesting.
The matrix models that were presented do not seem near a solution, but would be very interesting to study. Finding a generalization of the character expansion method by Kazakov et al. [34] for a condition that mixes two external matrices would open up a whole new class of possibly solvable coloured matrix models.
It might be the case that a map from either of the gCDT models to a controllable ensemble can be found. There is however a certain amount of conservation of difficulty involved, as the combinatorics of bubbles and strips and the complicated light cone colouring condition will always play a role. This is therefore an approach that is not very likely to render a solution. On the other hand, when it comes to maps between geometric ensembles, it seems that anything is possible.
Advanced graph theory might present a solution, although many results from this field do not seem applicable.
The most promising approach at this point is to study the model numerically using Monte Carlo simulations. Although this will not present an analytical result, it would presumably

be able to answer the question whether this model yields the same continuum behaviour as CDT in two dimensions, whether it possesses a well-defined limit at all, and in which regions of the phase space such a continuum limit would present itself.

Acknowledgements

First of all I would like to thank my physics supervisor Renate Loll, who has been an inspiration and a role model for me during the past few years. To my mathematics supervisor Tom Ilmanen I am very grateful for our enjoyable conversations about mathematics and life. I would like to thank my second mathematics supervisor Gunther Cornelissen for stepping in at the last moment and being very helpful with the project.
Samo Jordan, thanks for the nice discussions and for the ideas that sparked this interesting project. I would also like to thank Dario Benedetti and Razvan Gurau for a few interesting discussions concerning the matrix models presented here.

I would like to thank my parents for their eternal love and support, my mother Anneke Kerkhof in particular for the comforting cups of coffee in town at vital moments during this difficult year and my father Dick Hoekzema for sparking my curiosity ever since I was a little girl. Thanks to my sisters Elseline and Tessa and my little nephew Timo and newborn niece Jasmijn, for reminding me what is really important in life. I thank my parents in law, Ike van den Berg and Jos Wasserman, and my friends, in particular Vivian Jacobs and Alje Boonstra, for their support. Last but not least, Thomas Wasserman, my partner in love and science, thank you for everything.

For questions or comments concerning the contents of this thesis please contact me at the given e-mail address.

References

[1] M.E. Agishtein and A.A. Migdal, *Critical behavior of dynamically triangulated quantum gravity in four-dimensions*, Nuclear Physics B **385** (1992), 395–412.

[2] J. Ambjørn, *CDT as a scaling limit of matrix models*, Arxiv preprint arXiv:1105.1741 (2011).

[3] J. Ambjørn, J. Barkley, T. Budd, and R. Loll, *Baby universes revisited*, Physics Letters B **706** (2011), no. 1, 86–89.

[4] J. Ambjørn, J. Correia, C. Kristjansen, and R. Loll, *The relation between Euclidean and Lorentzian 2D quantum gravity*, Physics Letters B **475** (2000), no. 1-2, 24–32.

[5] J. Ambjørn, B. Durhuus, J. Fröhlich, and P. Orland, *The appearance of critical dimensions in regulated string theories*, Nuclear Physics B **270** (1986), 457–482.

[6] J. Ambjørn, A. Görlich, S. Jordan, J. Jurkiewicz, and R. Loll, *CDT meets Hořava-Lifshitz gravity*, Physics Letters B **690** (2010), 413–419.

[7] J. Ambjørn, A. Görlich, J. Jurkiewicz, and R. Loll, *Nonperturbative quantum de Sitter universe*, Physical Review D **78** (2008), no. 6, 063544.

[8] ———, *Planckian birth of a quantum de Sitter universe*, Physical Review letters **100** (2008), no. 9, 91304.

[9] J. Ambjørn, A. Görlich, J. Jurkiewicz, and R. Loll, *Nonperturbative quantum gravity*, Arxiv preprint arXiv:1203.3591 (2012).

[10] J. Ambjørn and J. Jurkiewicz, *Four-dimensional simplicial quantum gravity*, Physics Letters B **278** (1992), no. 1, 42–50.

[11] J. Ambjørn, J. Jurkiewicz, and R. Loll, *Dynamically triangulating Lorentzian quantum gravity*, Nuclear Physics B **610** (2001), no. 1, 347–382.

[12] ———, *Reconstructing the universe*, Physical Review D **72** (2005), no. 6, 064014.

[13] J. Ambjørn and R. Loll, *Non-perturbative Lorentzian quantum gravity, causality and topology change*, Nuclear Physics B **536** (1998), no. 1, 407–434.

[14] J. Bang-Jensen and G. Gutin, *Digraphs: theory, algorithms and applications*, Springer Verlag, 2009.

[15] D. Benedetti and J. Henson, *Imposing causality on a matrix model*, Physics Letters B **678** (2009), no. 2, 222–226.

[16] Daniel Bienstock and Michael A. Langston, *Chapter 8 Algorithmic implications of the graph minor theorem*, Network Models (C.L. Monma M.O. Ball, T.L. Magnanti and G.L. Nemhauser, eds.), Handbooks in Operations Research and Management Science, vol. 7, Elsevier, 1995, pp. 481 – 502.

[17] B. Bollobás, *Modern graph theory*, vol. 184, Springer Verlag, 1998.

[18] Luca Bombelli, Joohan Lee, David Meyer, and Rafael D. Sorkin, *Space-time as a causal set*, Physical Review Letters **59** (1987), 521–524.

[19] D.V. Boulatov, V.A. Kazakov, I.K. Kostov, and A.A. Migdal, *Analytical and numerical study of a model of dynamically triangulated random surfaces*, Nuclear Physics B **275** (1986), no. 4, 641–686.

[20] F. David, *Simplicial quantum gravity and random lattices*, Arxiv preprint arXiv:hep-th/9303127 (1993).

[21] P. Di Francesco, *2D quantum gravity, matrix models and graph combinatorics*, Applications of random matrices in physics (2006), 33–88.

[22] P. Di Francesco, P. Ginsparg, and J. Zinn-Justin, *2D Gravity and Random Matrices*, Physics Reports **254** (1995), no. 1, 1–133.

[23] P. Di Francesco, E. Guitter, and C. Kristjansen, *Integrable 2D Lorentzian gravity and random walks*, Nuclear Physics B **567** (2000), no. 3, 515–553.

[24] F. Dowker, *Topology change in quantum gravity*, Arxiv preprint arXiv:gr-qc/0206020 (2002).

[25] B. Durhuus, T. Jonsson, and J.F. Wheater, *On the spectral dimension of causal triangulations*, Journal of Statistical Physics **139** (2010), no. 5, 859–881.

[26] B. Eynard, *Random Matrices*, Saclay Lecture Notes (2000).

[27] J. Henson, *Discovering the Discrete Universe*, Arxiv preprint arXiv:1003.5890 (2010).

[28] P. Hořava, *Quantum gravity at a Lifshitz point*, Physical Review D **79** (2009), no. 8, 084008.

[29] C. Isham, *Prima facie questions in quantum gravity*, Canonical Gravity: From Classical to Quantum, Lecture Notes in Physics, vol. 434, Springer, 1994, pp. 1–21.

[30] ———, *Structural issues in quantum gravity*, Arxiv preprint gr-qc/9510063 (1995).

[31] ———, *Some reflections on the status of conventional quantum theory when applied to quantum gravity*, Arxiv preprint arXiv:quant-ph/0206090 (2002).

[32] S. Jordan and R. Loll, *in preparation*.

[33] V.A. Kazakov, M. Staudacher, and T. Wynter, *Almost flat planar diagrams*, Communications in Mathematical Physics **179** (1996), no. 1, 235–256.

[34] ———, *Character expansion methods for matrix models of dually weighted graphs*, Communications in Mathematical Physics **177** (1996), no. 2, 451–468.

[35] V.A. Kazakov and P. Zinn-Justin, *Two-matrix model with ABAB interaction*, Nuclear Physics B **546** (1999), no. 3, 647–668.

[36] A. Krzywicki, *Random manifolds and quantum gravity*, Nuclear Physics B-Proceedings Supplements **83** (2000), 126–130.

[37] Renate Loll, *A Discrete History of the Lorentzian Path Integral*, Quantum Gravity, Lecture Notes in Physics, vol. 0631, Springer, 2003, pp. 3–13.

[38] M. Petkovšek, H.S. Wilf, and D. Zeilberger, *A=B*, A. K. Peters, Ltd., 1997.

[39] T. Regge, *General relativity without coordinates*, Il Nuovo Cimento (1955-1965) **19** (1961), no. 3, 558–571.

[40] V. Rivasseau, *Constructive matrix theory*, Journal of High Energy Physics **0709** (2007), 008.